Winter 12-7-2020

Performance Improvements for Next Generation Falling Particle Receiver Systems

Nathan R. Schroeder
University of New Mexico

Nathaniel Schroeder

Candidate

Mechanical Engineering

Department

This thesis is approved, and it is acceptable in quality and form for publication:

Approved by the Thesis Committee:

Gowtham Mohan, Chairperson

Peter Vorobieff

Clifford Ho

PERFORMANCE IMPROVEMENTS FOR NEXT

GENERATION FALLING PARTICLE RECEIVER SYSTEMS

by

NATHANIEL SCHROEDER

BSME, UNIVERSITY OF NEW MEXICO, 2018

THESIS

Submitted in Partial Fulfillment of the

Requirements for the Degree of

Master of Science in Mechanical Engineering

The University of New Mexico

Albuquerque, New Mexico

May 2021

ACKNOWLEDGEMENTS

I hereby acknowledge my advisor and committee chair, Gowtham Mohan, for sparking my interest in concentrating solar power systems. The enthusiasm shown in your course encouraged me to contribute to the fight against climate change in a way that I am truly passionate about.

I would like to thank Clifford Ho for his continued support in the development of my skills in engineering and problem solving. Without your relentless encouragement and unending patience, I would not have found the joy I have in my research.

To my parents, Pat and Sonja, you have given me the foundation to achieve my dreams. I owe everything I have accomplished to your loving support.

To my editor, best friend, and confidant, Kayleigh Maes, your love has given me the motivation to keep working through good times and bad. Through the long weekends of writing and the daily humdrum of research, you have been the light that keeps my head out of the clouds.

Performance Improvements for Next Generation Falling Particle Receiver Systems

by

Nathaniel Schroeder

BSME, Mechanical Engineering, University of New Mexico, 2018

MSME, Mechanical Engineering, University of New Mexico, 2021

ABSTRACT

Falling particle receiver (FPR) systems are a rapidly developing technology for concentrating solar power applications. Solid particles are used as both the heat transfer fluid and thermal energy storage media. Through the direct solar irradiation of the solid particles, flux and temperature limitations of tube-bundle receives can be overcome leading to higher operating temperatures and energy conversion efficiencies. Particle residence time, curtain opacity, and curtain stability affect the performance of FPR designs. As the particles fall through the receiver the curtain accelerates, increasing its transmissivity thus decreasing the amount of energy absorbed. Multistage release trough structures catch and release the particles to decrease their downward velocity and regroup the freefalling curtain thus increasing curtain opacity and particle residence time while also improving curtain stability. A novel Staggered Angle Iron Receiver (StAIR) multistage release concept was tested at a small scale before being implemented in a 1 MW_{th} receiver. The sloped angle

iron troughs feature a front lip that accumulates the falling particles allowing subsequent particles to spill over thus passively decelerating the particles and ensuring a more stable curtain behavior.

The effect the staggered angle iron geometry, vertical position, horizontal position, and orientation have on curtain transmissivity were studied at linear mass flow rates between 3.9 and 11.8 kg/s per meter of curtain width. Curtain transmissivity was measured 12" below a trough and compared to the freefalling curtain of the same mass flow rate. Trough vertical position and geometry had a larger effect on curtain transmissivity than trough orientation and horizontal position. A hybrid trough geometry located 36" from the curtain origin at a mass flow rate of 4.1 kg/m/s resulted in the largest gain in curtain opacity when compared to a freefalling curtain with an opacity of 60% for the freefalling curtain and 86% for the curtain following the trough. Two and three troughs were then tested in series to determine their effect on particle bounce and transmissivity. An optimal trough position and geometry was selected to be tested in an on-sun 1 MW_{th} receiver test campaign. Cold flow tests inside the receiver were conducted to ensure particle attrition through the receiver aperture was not significantly higher than that of a freefalling curtain. On-sun testing was conducted with one and two trough configurations. Receiver efficiency and back wall temperatures were measured to determine the StAIRs performance.

TABLE OF CONTENTS

LIST OF FIGURES

LIST OF TABLES

CHAPTER 1

BACKGROUND

2.1 Concentrating Solar Power History

Concentrating solar power tower systems have evolved since the construction of the world's first solar tower testing ground, the National Solar Thermal Test Facility, built in the 1970s. Early tower designs heated steam to directly spin a turbine. Later generations used molten nitrate salts as a heat transfer fluid to store the thermal energy. In these CSP systems, molten salt is pumped through an array of tubes (receiver) to be heated by the concentrated solar flux before entering a hot storage container. The molten salt is passed from the hot storage bin to a cold storage bin through a water/salt heat exchanger powering a steam Rankine turbine. [1]

Solar 1 and Solar 2 were the first CSP tower systems to generate electricity at a commercial scale. Solar 1, operating from 1982 to 1986, was the first concentrating solar tower of its kind heating water directly through a tube bank receiver to power a Rankine cycle turbine. This lead to the development of PS10 in Spain, a 11MW saturated steam CSP system which includes 50 minutes of thermal energy storage at 50% load. [2] The use of high pressure steam as a systems thermal energy storage has multiple design limitations making it difficult to store more than an hours' worth of energy.

After Solar 1's successful operation, thermal storage was introduced in the form of a molten mixture of 60% sodium nitrate ($NaNO_3$) and 40% potassium nitrate (KNO_3) salt. While Solar 1 was only able to produce electricity during the day, Solar 2 allowed for the

production of electricity overnight or on cloudy days with the introduction of the molten salt thermal energy storage. Both systems provided the proof of concept for solar power tower technology producing $10MW_{el}$ each. [3]

While molten salt systems do provide thermal storage, it came with difficulties containing high-temperature corrosive fluid and maintaining the temperature of the fluid above its freezing point, 250 ° C. Costly trace heating and instability at temperatures above 530°C introduce the need for a more stable heat transfer fluid such as ceramic particles. [4]

2.3 Falling Particle Receivers

Falling Particle Receivers (FPR) utilize a solid heat transfer fluid to absorb solar irradiance for the generation of power or use in process heating applications. The particles are cascaded through a slide gate to freefall as a curtain into a cavity receiver and absorb incident solar irradiance. FPRs were first considered in the early 1980s with experiments using 650 μm particles. Falling particle characteristics including, particle velocity, volume fraction, entrained airflow, and convective heat transfer were considered. Particle curtain freefall terminal velocity increases when compared to the terminal velocity of individual particles decreasing the potential particle residence time inside a receiver. [5]

Solid particles can directly absorb incident solar flux and serve as a system's thermal storage medium. Candidate particles for a falling particle receiver were first tested considering particle absorptance, transmittance, and reflectance. Proppants used in oil extraction processes were considered due to their high absorptivity and stability at temperatures >1000°C. Stahl *et al.* conducted some of the initial optical tests on Norton Masterbeads which were composed of alumina oxide (Al_2O_3.) [6]

Kim K *et al.* conducted experiments with a freefalling curtain using particle diameters of 300, 697, and 1291 μm to determine particle curtain opacity, thickness, and velocity. It was found that the 300 μm particles had an increased curtain opacity when compared to the larger, 697 and 1291 μm, particles. A tradeoff between opacity and wind effect is present where falling particle curtains containing larger diameter particles, 697 and 1291 μm, are not as easily disturbed by the presence of air currents as particle curtains containing 300 μm particles. Particle velocity increased with increased distance from the curtain origin which resulted in a decrease in the particle solid fraction. The maximum solid particle volume fraction for 690 μm particles flowing at 4.2 kg/m/s was ~2.5% 30 cm below the discharge slot decreasing to 1% as the particles reached terminal velocity. Lower mass flow rates of 1.2 and 2.9 kg/m/s yielded solid volume fractions as low as .2% and .1% respectively. [7]

Initial on sun testing for falling particle receivers was conducted at the National Solar Thermal Test Facility, NSTTF, at Sandia Labs in Albuquerque, NM. Siegel *et al* designed and built a 2.5 MW_{th} receiver to determine falling particle receiver efficiencies. The design used a "batch mode" receiver without a means to recirculate particles. Particle receiver inlet temperatures were measured with particle receiver outlet temperatures to determine the change in temperature the particle experienced when freefalling through the solar flux. Particle outlet temperatures were limited to 300 ° C due to the ambient temperature of the particles at the receiver inlet. This batch mode approach resulted in peak receiver efficiencies of 50%. [8]

Testing continued at the NSTTF with the introduction of a 1 MW_{th} recirculating particle receiver design using an Olds, auger type, elevator. Particles in this system were dropped through a receiver via a slide gate, gathered in a bottom hopper, and elevated to a top

hopper to be dropped again. This design allowed for the study of higher particle inlet temperatures as the particles were heated with each successive drop through the receiver. Peak efficiencies of 70% were measured for the free-falling particles. In both receiver tests conducted at the NSTTF a sintered bauxite particle, CARBO Accucast ID 50, with a nominal diameter of ~280 μm was used. [9]

2.4 Obstructed Flow

Obstructed flow testing was conducted using the $1MW_{th}$ receiver at the NSTTF. An array of chevron-shaped stainless-steel mesh structures was implemented in the receiver to slow the particle curtain, increase flow stability, and increase the solid mass fraction. While this configuration resulted in maximum efficiencies of 80 %, significant degradation of the stainless-steel structures occurred due to particle wear and exposure to high irradiances. [9]

Lee *et al* had tested the flowability of particles through a metallic porous structure to slow particle decent to be tested on-sun. Mass flow rates were determined for white sand and Accucast ID 50 proppants through a structure with the same porosity. Particles were shown to flow through the porous media without clogging even with the introduction of multiple porous blocks. [10]

Centrifugal particle receivers have been designed and tested on-sun at Juelich Solar Tower in Germany. Centrifugal particle receivers increase particle dwell time by rotating a cylindrical cavity in which the particles are exposed to the solar flux. Particles descend the downward nod of the receiver along the receiver walls due to the centrifugal force of the rotating drum. The rotational speed is used to control particle residence time. A prototype

2.5 MW_{th} receiver was able to achieve particle outlet temperatures of 990 ° C at mass flow rates of .07 - .18 kg/s. [11]

Multistage catch and release structures were investigated by JS Kim *et al*. Simulations and experiments using multiple troughs to catch and release a particle curtain were conducted with particle diameters of 280 μm and 697 μm. Simulations had shown a decrease in the particle volume fraction following the troughs when compared to a freefalling curtain at the same location. The mass flow rate of the curtain falling through a receiver dictates the necessity of the multistage falling. A curtain composed of 280 μm particles and a lower mass flow rate, <15 kg/s/m, benefit from the troughs as the absorptivity increase is more significant. Curtains composed of 697 μm particles show an increase in absorptivity for mass flow rates ranging from 0-30 kg/s/m. [12]

Wind has a significant effect on open cavity FPR systems as curtain behavior is affected by the presence of airflow. Kim *et al* modeled particle attrition through a receiver aperture as a function of wind speed, direction, and cavity depth. Wind speeds greater than 6.5 m/s, at an angle of attack of 45 ° to the aperture, and a cavity depth of .46 m resulted in the largest amount of particle loss. Receivers with a back wall close to the particle curtain experience less particle loss in the presence of wind. [13]

CHAPTER 2

INTRODUCTION

1.1 Motivation

Concentrating Solar Power, CSP, can take many forms. From line focus, mirrored trough systems to point focus, dish and tower systems. This paper will focus on tower systems which can be categorized as Generation 1 or Generation 2 systems. Generation 1 systems heat water in a tube bank receiver to generate steam to directly power a steam Rankine cycle. Generation 2 systems heat molten salt in the tube bank receiver to achieve higher temperatures and serve as the system's thermal energy storage for power generation overnight. [14]

Molten salt CSP systems are currently operational around the world; examples of this technology are Solana Generating Station in Arizona and Ivanpah in California, parabolic trough and tower systems, respectively. Most molten salt chemistries have a maximum operating temperature of ~550°C greater than which the salt begins to decompose. [1]

Current CSP generation around the world totals 6126 MW with another 3139 MW under construction or in development. Many of these systems utilize molten salt as the heat transfer and storage medium with a LCOE of .13-.17 dollars/kWh [15]

The US Department of Energy, through the SunShot program, has set a goal of $.06 per kWh to make the next generation of CSP systems competitive in today's power market. Generation 3 Concentrating Solar Power (Gen3CSP) towers seek to utilize a new form of heat transfer and storage media that can operate at a wider range of temperatures compared

to the Generation 2 molten salt systems. [14] Three new heat transfer fluids (HTF) are being considered for this 3rd generation CSP systems: sCO2(gaseous/supercritical pathway), molten chloride salt mixture and molten sodium (liquid pathway), and particles (solid pathway). Temperatures greater than 700 ° C allow for the use of more efficient power cycles, such as the supercritical CO_2 Brayton cycle that can boost efficiency (up to 10 % when compared to traditional steam Rankine cycles) and decrease the LCOE of concentrating solar power systems. [16]

Falling particle receivers (FPR) utilize solid particles as HTF and thermal energy storage (TES). Particles on the order of hundreds of microns can be treated as quasi-fluid as they can flow in the direction of gravity. This behavior is advantageous to create a gravity-fed system that does not require the use of pumps or valves. The particles can be lifted using equipment from mining operations, such as bucket elevators, screw elevators, or skip hoists modified to handle high-temperature material. Particle flow can be controlled using linear actuated slide gates. This reduces the cost associated with high-temperature corrosive resistant valves and pumps used in molten salt CSP systems.

Figure 1: Falling Particle Receiver. [17]

Falling particle systems release a curtain of particles from a top hopper into a cavity receiver to absorb incident solar flux directly, negating the need for tube bank containment,

Figure 1. From the receiver, the particles flow to a hot storage bin before being passed through a particle/sCO2 heat exchanger to power an sCO2 turbine. A cold storage bin then

holds the particles before an elevator lifts them back up to the top hopper above the receiver.

In freefalling particle receivers, curtain stability and curtain density decrease with increasing drop distance. As the particles downward velocity increases the solid volume fraction of the curtain increases. Maintaining higher solid volume fraction, and thus high curtain opacity, increases the absorptance of the curtain which intern increases the efficiency of the receiver. [7] Multistage catch and release structures decrease the downward velocity of the particle curtain though the interruption of the curtain's flow in the receiver. The introduction of catch and release structures has the potential to create higher curtain opacity and stability when compared to a freefalling curtain. A novel multistage catch and release, Staggered Angle Iron Receiver (StAIR), Figure 2, concept is explored in this paper with the purpose of increasing particle curtain opacity and stability resulting in higher receiver efficiencies.

Figure 2: Staggered Angle Iron Receiver (StAIR) multistage release with 2 troughs

1.3 Objectives

The objectives of this study are to test the StAIR concept at small scale using a bench scale test rig, determine the optimal trough geometry out of four candidates with varying orientation, vertical position, and horizontal position by measuring curtain transmissivity, and implement the down selected trough in a 1 MW_{th} falling particle receiver to compare with receiver efficiencies and back wall temperatures measured using a freefalling particle curtain.

1.4 Achieved Results

Particle curtain stability and opacity was significantly improved compared to a freefalling curtain through the implementation of multistage StAIR concept at small scale. An optimal trough geometry, position, and orientation was determined. Design and implementation of an adjustable test apparatus inside a 1 MW_{th} falling particle receiver resulted in the successful operation of multiple trough configurations through cold flow and on-sun testing. Receiver efficiencies of 85%-90% were achieved with minimal heating of the receivers back wall in both one and two trough configurations. Theoretical maximum receiver efficiencies were calculated as a function of incident power for particle temperatures of 350-750°C to help validate the on-sun efficiency measurements.

1.5 Thesis Outline

In this paper, the investigation of a staggered angle iron receiver concept will be outlined. Chapter 3 covers the bench-scale testing of the stAIR design in which the methods, theory, and results are discussed. On-sun testing is explored in Chapter 4 with an analysis of the

parameter space, theoretical maximum efficiencies, test procedure, and results. Chapter 5 contains the conclusions of this paper with a summary of the FPR's performance with the modifications implemented in the Summer and Fall of 2020.

CHAPTER 3

STAGGERED ANGLE IRON RECEIVER BENCH SCALE TESTING

3.1 Approach

A test stand was constructed with an upper bin and linear actuated slide gate coving a 6” wide slot, Figure 3. The thickness of the curtain was set using a travel limiter on the linear actuated slide gate allowing for an adjustable mass flow rate from 2-15 kg/m/s. Two slot depths, ¼” and ½”, corresponding to 3.9-4.1 kg/m/s and 9.8-11.8 kg/m/s respectively, were chosen for the test campaign. Mass flow rates were documented in kg/m/s for comparability to a one meter wide curtain in the 1 MW FPR. A lower bin was positioned at the bottom of the test stand allowing for 48” of drop distance from the slide gate. A load cell below the lower bin was used to measure the curtain's mass flow rate. An adjustable arm held the lux meter at the rear of the test stand to measure curtain transmissivity. Two 600-watt metal halide floodlights were placed on the opposite side of

Figure 3: Particle curtain test stand with 3 stAIRs

the particle curtain to act as a light source for the lux meter. Cameras were placed to capture the curtain's behavior from a front and profile view.

Lux measurements were taken at curtain heights of 12”, 24”, 36”, and 48” for both freefall and trough interrupted flow. Lux measurements were gathered 12” from the bottom of the trough during each experiment with an example shown in Figure 4.

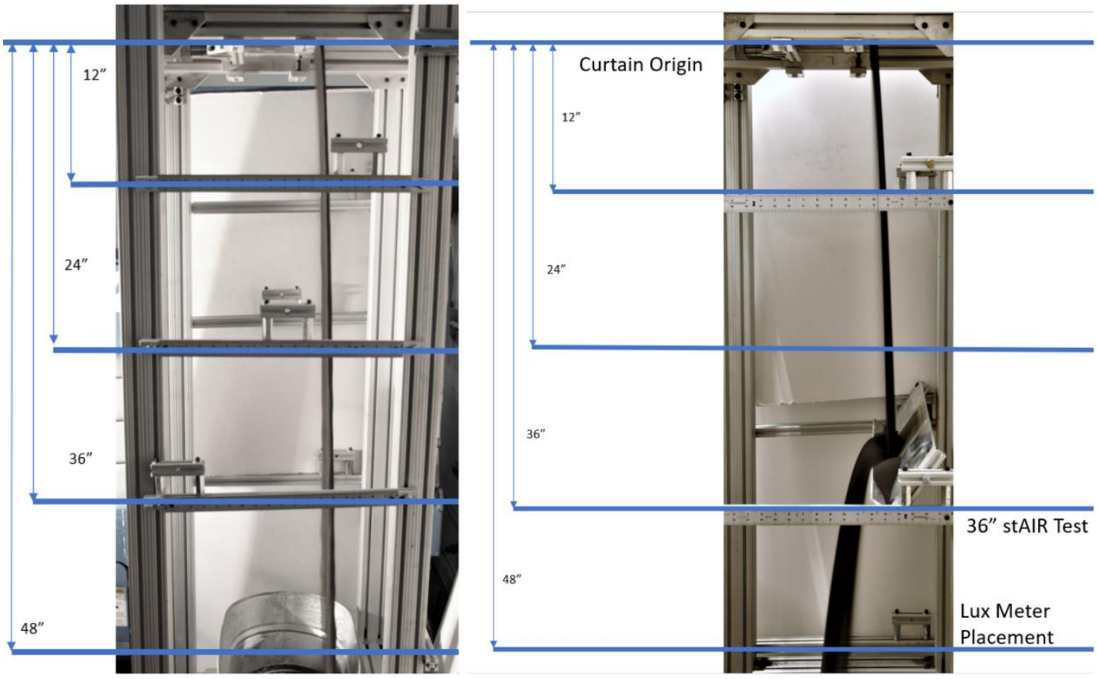

Figure 4:Test stand profile showing curtain drop height(left) and lux meter placement in relation to the trough(right) at a 36” vertical position.

Twelve troughs were constructed, three of each of the four geometries shown in Figure 5. Adjustments to the vertical distance from the curtain origin, horizontal position with respect to the curtain, and trough orientation can be made to each of the three troughs using the supporting members. The diagram shown in Figure 5 (2) demonstrates the permutations of horizontal position and orientation of the troughs for each geometry. Each trough configuration was tested at both ½” and ¼” slot depths. The 90 and 120-degree angle irons were positioned with respect to the location of the curtain and the

vertex of the angle iron. “On-V” refers to the curtain impinging in the vertex of the angle iron, “V+1” implies the curtain impinges one inch from the vertex, while “V+2” refers to the curtain impinging two inches from the vertex towards the back edge. The flat bottom trough was tested at three horizontal locations each ½” apart with the center position in line with the center of the trough. Hybrid troughs were tested in one horizontal position due to constraints on the test stand.

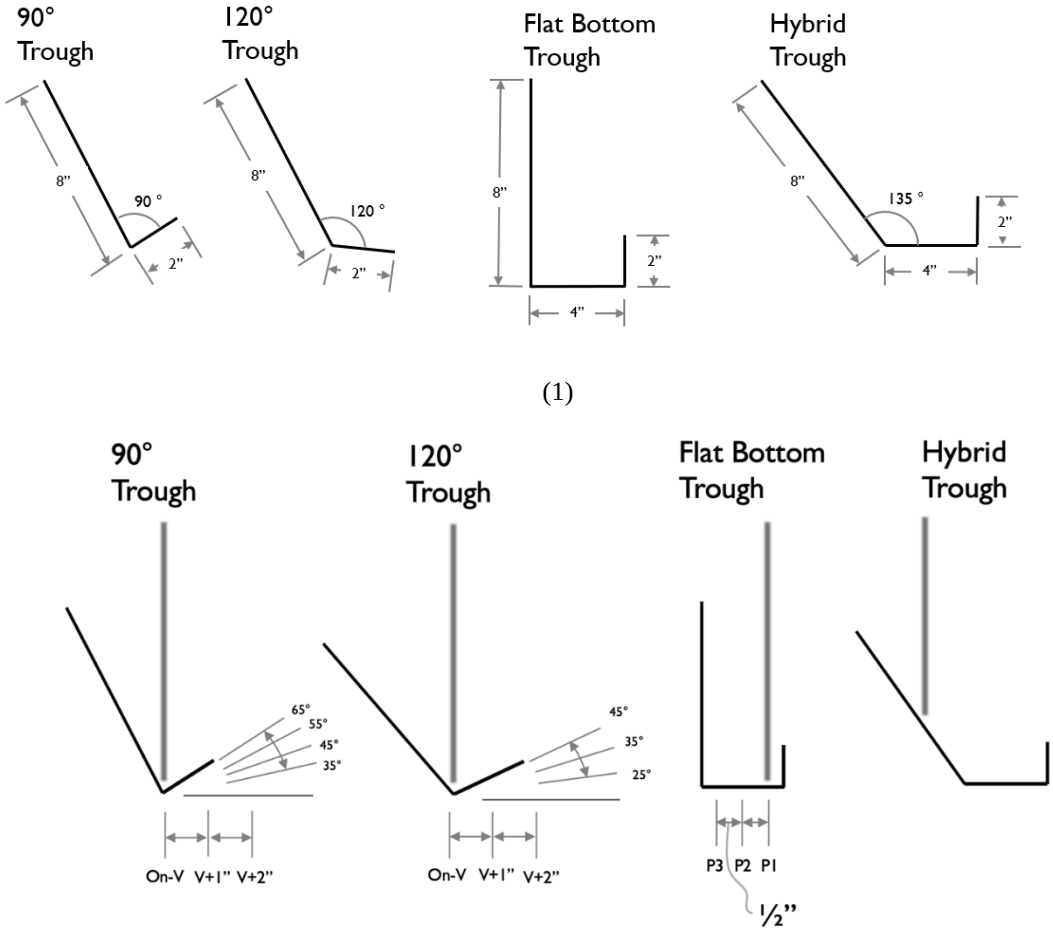

Figure 5: (1) Trough geometries and dimensions. (2) Trough horizontal positions and orientations with respect the particle curtain

The orientation of the 90-degree trough ranged from 35° to 65°, with respect to horizontal, in 10° increments while the 120-degree angle iron tested in orientations ranging from 25°

to 45° in 10° increments. The orientation ranges were chosen due to their ability to gather a particle pile without spilling particles off the back edge of the trough.

Each trough geometery was tested at 12”, 24”, and 36” from the curtain origin in each pertumetation of horizontal position and orientation.

An optimal trough geometry and configuration was selected to continue in two trough testing. The down selected trough was kept 12” vertical distance from the curtain origin while a second trough of the same geometry was tested 12” and 24” below the first with varying orientation and horizontal position.

Curtain transmissivity was measured by determining the amount of light that passed from the floodlamps through the curtain to the lux meter. To prevent contamination from background light sources and light that did not pass through the curtain, an equation for curtain transmissivity was derived.

$$\tau = \frac{q''_{\text{c,lights}} - q''_{\text{c,nolights}}}{q''_{\text{lights}} - q''_{\text{nolights}}} \qquad (1)$$

Where τ(%) is the light generated by the lamps transmitted through the particle curtain expressed as percentage of incident light, $q''_{\text{c,lights}}$ (lux) is the light detected by the sensor with the lamps on while the curtain is in place, $q''_{\text{c,nolights}}$ (lux) is the light detected by the senor without the lamps while the curtain is flowing, q''_{lights} (lux) is the light detected by the sensor with the lamps on without the curtain, and q''_{nolights} (lux) is the light detected by the sensor with the lamps off without the curtain. Figure 6 shows the light being detected by the lux meter used the calculation of transmittance. The thin blue lines represent background light while orange thick lines represent light produced by the halogen lamps. Light that has not passed through the curtain is indicated by solid lines. Dashed lines

indicate light that has passed through the particle curtain. Where $q''_{c,lights}$ is the dotted thick/orange lines, $q''_{c,nolights}$ is the dotted thin/blue lines, q''_{lights} is the solid thick/orange lines, and $q''_{nolights}$ is the solid thin/blue lines.

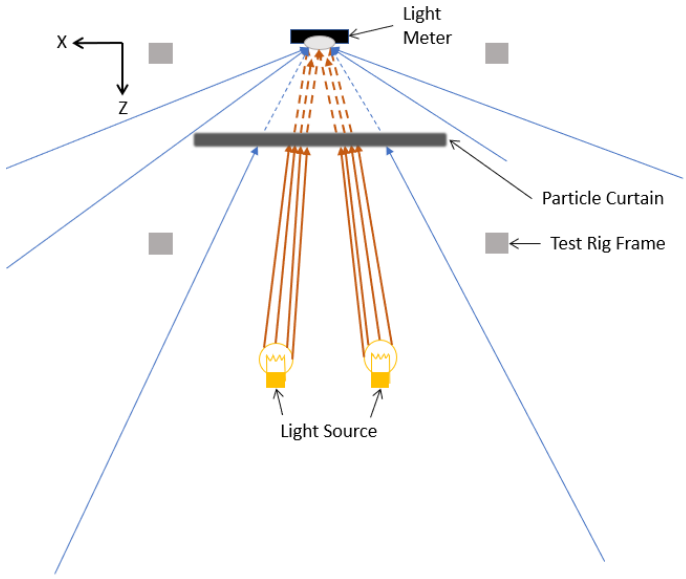

Figure 6: Light measured by the lux meter.

Images collected by the cameras gave insight into how much particle bounce was occurring off the top of the particle pile. Longer exposures of 1/40 of a second create streaks indicating particle paths off of the trough. Particle bounce can then be compared qualitatively between trough geometries, positions, and orientations.

3.1.2 Results

3.1.2.1 Trough Orientation and Geometry Down Select

Measurements were taken of a freefalling curtain using the prescribed slot depths of ¼" and ½" for comparison with the trough interrupted curtain. Figure 7 shows the curtain transmissivity as a function of drop distance for both a 4.1 kg/m/s an 11.7 kg/m/s mass

flow rate. Transmissivity of the curtain flowing at 4.1 kg/m/s decreases as function of drop height at a higher rate than that of a curtain flowing at 11.7 kg/m/s. A troughs performance can be considered favorable if the curtain following the trough has a transmissivity lower than that of the freefalling curtain of the same mass flow rate and drop distance.

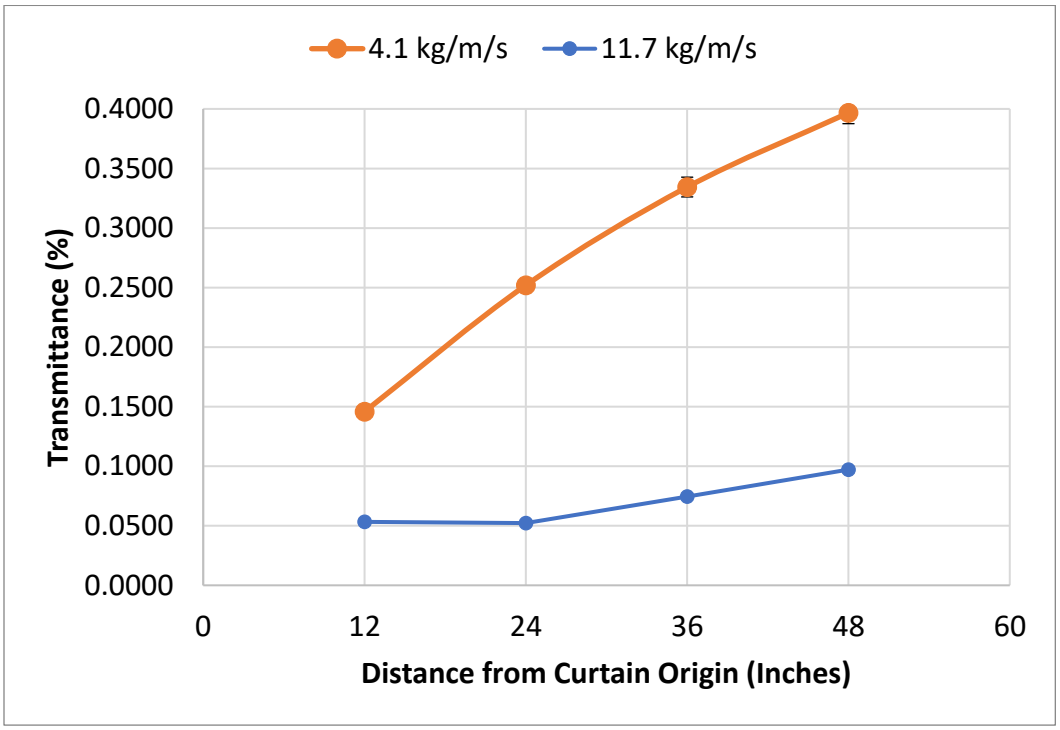

Figure 7: Freefall curtain transmittance as a function of drop distance for 4.1 and 11.6 kg/m/s mass flow rates

3.1.2.2 Particle mass flow rate = 3.8-4.1 kg/m/s

Figure 8 shown curtain transmissivity for the 90-degree and 120-degree angle irons, flat bottom trough, and hybrid trough. Yellow, dotted/dashed, lines represent troughs located 36" below curtain origin with blue, solid, lines representing 24", and green, dashed, lines 12". Horizontal positions are distributed on the x-axis with transitivity on the y-axis. Horizontal lines spanning all 4 graphs represent the transmissivity of a curtain in freefall in the same vertical location. Lines of the same color on the 90-degree and 120-degree trough graphs represent trough orientations which had less of an effect on curtain

transmissivity. At slot depth of ¼", correlated to a measured mass flow rate between 3.8 and 4.1 kg/m/s, trough orientation and horizontal position was found to have the least effect on curtain transmissivity when compared to vertical position and trough geometry with the maximum change in transmissivity of 5% between orientations and 5% between horizontal position.

The 90-degree angle iron oriented at 65° resulted in a curtain with a transmissivity lower than that of the 35°, 45°, and 55° orientation at the least transmissive horizontal position. Trough orientation had a decreasing effect on the curtain's opacity with a larger drop distance to the first trough. The maximum difference in transmissivity compared to a freefalling curtain for a 90-degree angle iron placed 12", 24", and 36" from the curtain origin were 1%, 11%, and 20% respectively. At vertical distances of 24" and 36" trough orientations resulted in statistically similar curtain transmissivities. For a given orientation 12" below the curtain origin the on-V horizontal position resulted in the least transmissive curtain with up to a ~5% and ~7% increase in opacity when compared with the V+1 and V+2 position respectively. Changes to curtain transmissivity between horizontal position decreased with increasing curtain drop distance to the trough. The optimal configuration for the 90-degree trough was a 65° orientation, on-V horizontal position, and 36" distance from the curtain origin with a 20% decrease in curtain transmissivity compared to freefall.

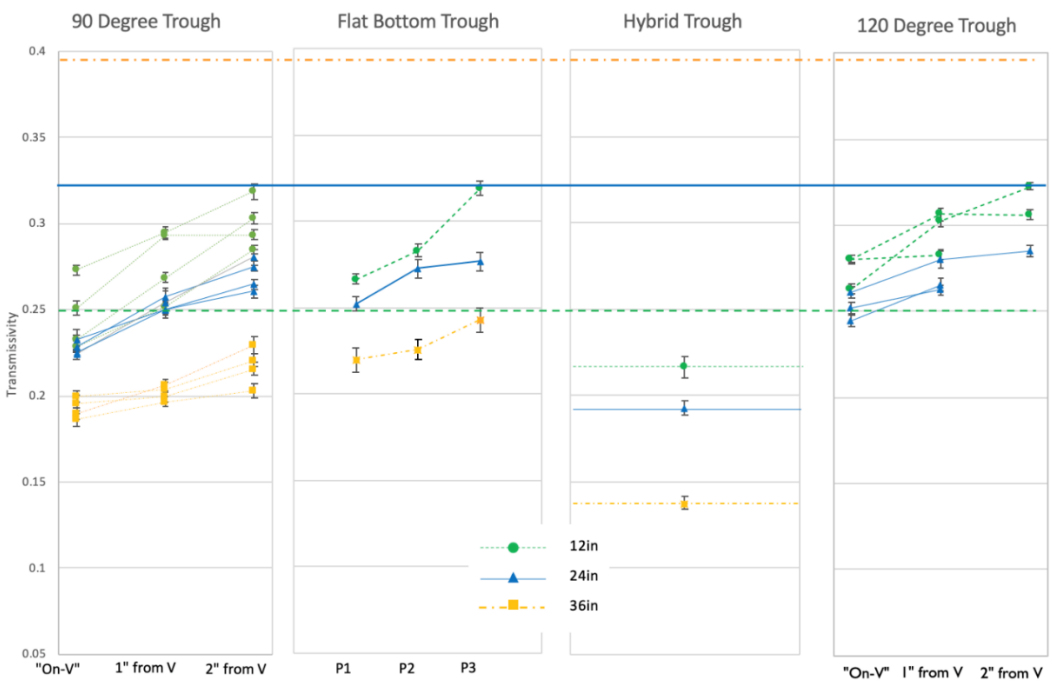

Figure 8: Curtain transmissivity measured 12" below the trough for a ¼" curtain aperture, corelated with a mass flow rate of 3.9-4.1 kg/m/s, for 90-degree and 120-degree angle iron, flat bottom trough, and hybrid trough..

The 120-degree angle iron oriented at 45° degrees resulted in a lower transmissivity than the 35° and 25° orientations. Orientation had less of an effect as the drop distance increased from 12" to 24". At a drop distance of 36" the particle pile spread out on the angle iron and began spilling over the back edge and was therefore excluded from the results. Curtain transmissivity was lower for a vertical position 24" from the curtain origin when compared to a 12". The optimal configuration of the 120-degree angle iron was a 45° orientation, on-V horizontal position, and 24" distance from curtain origin with a 7% decrease in curtain transmissivity compared to freefall.

Transmissivity was shown to decrease with front lip angles approaching 90° for both angle iron troughs. This led to the introduction of the flat bottom trough featuring a 90° front lip. The flat bottom trough was tested with 3 horizontal positions. In position 1, P1, the curtain impinged the particle pile ½" from the front lip of the trough, at P2 the curtain impinged at

the center of the trough, and P3 ½" from the rear. Position P1resulted in the lowest transmissivity followed by P2 and P3 respectively. As with the 90-degree and 120-degree angle irons the curtain following the flat bottom trough was the least transmissive compared to the freefalling curtain at 36" below the curtain origin. The optimal configuration for the flat bottom trough had a horizontal position P1, and a distance from the curtain origin of 36" which resulted in a curtain 16% less transmissive than a freefalling curtain.

The hybrid trough was only tested at 3.8-4.1 kg/m/s mass flow rate due to constraints on the test stand. The particle flow over this geometry followed the particle piles angle of repose, a ~30° angle from horizontal which is the steepest angle that can be formed by the particle pile without sliding. For all other trough designs tested the curtain bowed upward as it interacted with the particle pile close to the front lip. As the troughs were positioned with the curtain further from the front lip, from On-V to V+2, the Curtain Reaction At the Trough Ramp, CRATR, effect diminished resulting in a less opaque curtain and increased particle bounce. The hybrid trough was tested at 12", 24", and 36" from the curtain origin with a fixed horizontal position and orientation. At each vertical location the hybrid trough resulted in curtain transmissivity lower than that of the 90-degree, 120-degree, and flat bottom trough. The curtain transmissivity was lower than that of a freefalling curtain for each vertical position with a maximum difference in opacity of 25% at a drop distance of 36".

Comparing the 90-degree, 120-egree, and flat bottom troughs to a freefalling curtain shows that a trough 12" from the curtain origin increases transmissivity while troughs positioned 24" and 36" decrease the curtain's transmissivity. As a freefalling curtain accelerates

downward the solid volume fraction decreases meaning the curtain spreads and becomes less opaque with increasing drop distance, shown in Figure 7. If the trough is introduced closer than 24” from the curtain origin at mass flow rates of 3.8-4.1 kg/m/s, the curtain has not accelerated and spread enough to decrease its opacity and necessitate an interruption.

3.1.2.3 Particle mass flow rate = 9.8-11.8 kg/m/s

At a ½” slot opening, corelated to a mass flow rate 9.8-11.8 kg/m/s, orientation and horizontal position did not have a significant effect on curtain transmissivity compared to trough geometry and vertical position shown in Figure 9. Yellow, dotted/dashed, lines represent stAIRs located 36” below curtain origin with blue, solid, lines representing 24”, and green, dashed, lines representing 12”. Horizontal positions are distributed on the x-axis with transitivity on the y-axis. Horizontal lines spanning all 4 graphs represent the transmissivity of a curtain in freefall in the same vertical location. Lines of the same color on the 90-degree and 120-degree trough graphs represent stAIR orientations which had less of an effect on curtain transmissivity. Varying trough orientations had indeterminate effects on curtain transmissivity with a maximum difference between orientations of 2% in transmissivity.

The 90-degree and 120-degree angle iron orientation and horizontal position had little to no effect on the curtain transmissivity. Differences in transmissivity between orientations are attributed to test error due to inconsistent results. The V+1 horizontal position had shown a slight increase in transmissivity when compared to On-V and V+2 positions at a 12” drop distance yielding a 1-2% difference. The optimal 90-degree trough configuration of 35°, on-V horizontal location, and 36” distance from curtain origin resulted in a transmissivity ~1% less than freefall. The optimal 120-degree trough configuration of 25°

orientation, on-V, and 24” distance from curtain origin had a transmissivity 2% greater than freefall meaning the 120-degree angle iron had a negative effect on curtain opacity. The flat bottom trough position did not significantly affect curtain transmissivity. The optimal flat bottom trough configuration of P2 at 36” from the curtain origin resulted in a 2% less transmissive curtain.

The 12” and 24” drop distance for each of the trough geometry resulted in a less opaque curtain when compared to freefall. The trough positioned 36” from the curtain origin resulted in a more opaque curtain. This suggests that the freefalling curtain at this flow rate maintains a higher solid volume fraction when compared to the freefalling curtain with a 3.8-4.1 kg/m/s flow rate. A curtain with a mass flow rate of 9.8-11.8 kg/m/s interrupted by a trough <24” from the curtain origin will have a higher transmissivity than that of a freefalling curtain at the same location.

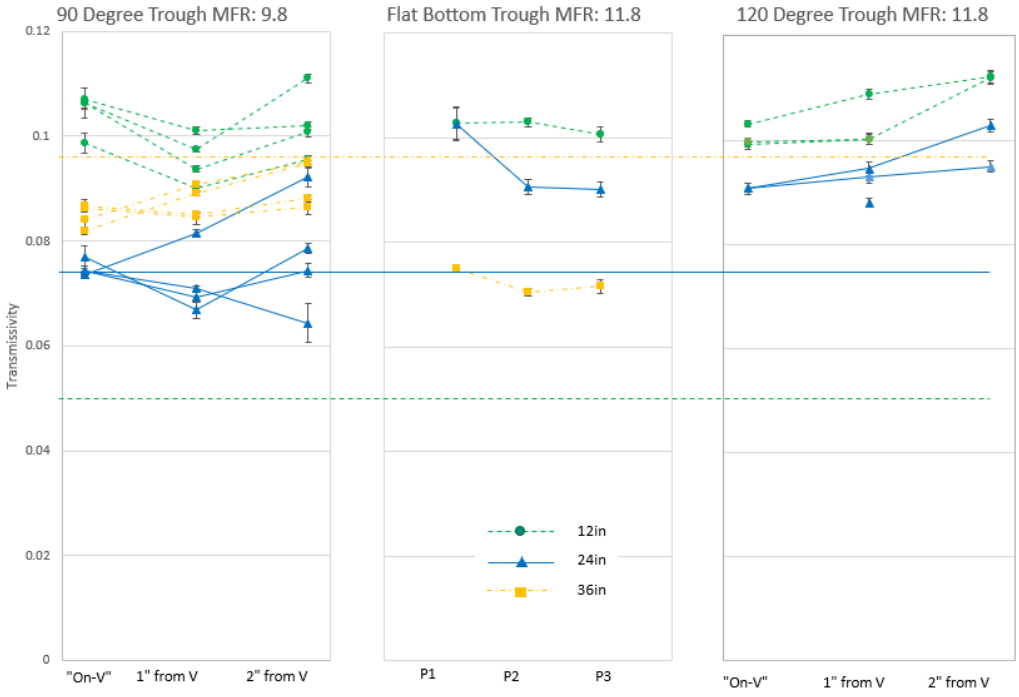

Figure 9: Curtain transmissivity measured 12” below the stAIR for a ½” curtain aperture corelated with a mass flow rate of 9.8-11.8 kg/m/s.

3.1.2.4 Multiple Troughs

A second trough was placed below the first for the 90 degree and flat bottom trough geometries. The first trough was kept at 12” from the curtain origin to allow for more vertical adjustment of the second trough. The second 90-degree angle iron and flat bottom trough were tested at 12” and 24” below the first with varying horizontal positions, ½” increments for the flat bottom trough

Figure 10: 2 trough configuration with a 4.1 kg/m/s mass flow rate. First trough 65 orientation, on-v position, 12" from curtain origin. Second trough 45 orientation, on-v position, 12" below the first. Particles can be seen bouncing at the second trough.

and 1” increments for the 90-degree angle iron. As the curtain left the first trough it began to spread out from the front lip, limiting changes to the second trough’s horizontal positions due to limited catchment area.

3.1.2.5 Multiple troughs at 3.9-4.1 kg/m/s

For the 90-degree trough, all configurations resulted in a curtain less transmissive than a freefalling curtain at the same location. Orientation and horizontal position did not have a significant effect on curtain transmissivity. Figure 11 shows the effect multiple stAIR configurations have on curtain transmissivity when compared to freefall. The two 90-degree trough case is shown on the right with the line of the same color representing different trough orientations. Yellow lines represent curtain transmissivity measured 48" below the curtain origin, black 39", blue 36", and green 32". Freefalling curtain transmissivity for 28" of drop height was not measured to compare with the 12" and 16" case.

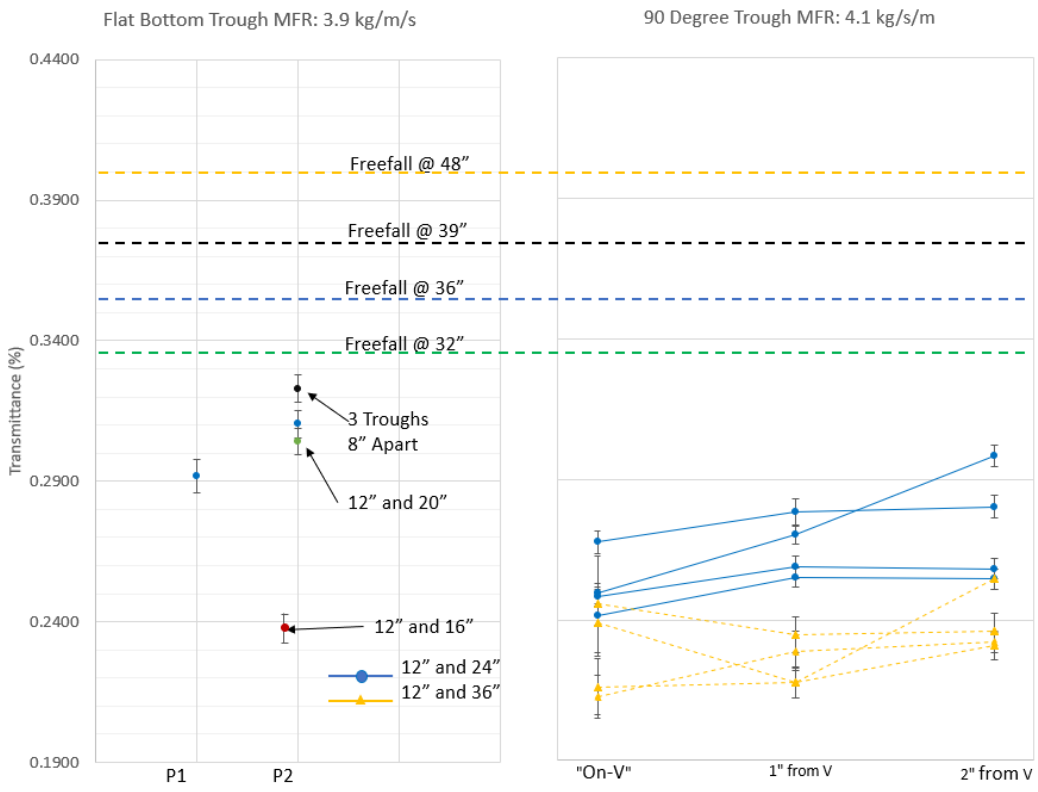

Figure 11: 2 trough configuration transmissivity compared to freefall

The curtain was less transmissive with the second trough placed 12” from the first when compared to the trough 24” from the first. However, the increased drop distance between troughs resulted in significantly higher particle bounce. The second trough configuration that resulted in a curtain 22% less transmissive than a curtain in freefall was oriented at 45°, a horizontal location of on-V, and a 24” distance from the first trough.

The flat bottom trough was only tested at two horizontal positions due to the limited catchment area of the second trough. The horizontal positions were found to have little effect on the transmissivity of the curtain. The flat bottom trough positioned 12” from the first resulted in a curtain 6% less transmissive than a freefalling curtain at the same location. Addition vertical positions 4” and 8” from the first trough were tested shown in Figure 11 and Figure 13. The profile of the curtain reveals that the particle bounce from the second trough is a function of its distance from the first trough with the least particle bounce occurring with the second trough positioned 4” from the first. Transmissivity at this second trough location was 7% less than that of a freefalling curtain.

3.1.2.6 Multiple troughs at 11.8 kg/m/s

Flat bottom troughs were selected for continued testing at mass flow rates of 11.8 kg/m/s due to their ability to catch and exclusively cascade particles over the front lip. 90-degree angle irons were found to spill particles off of the rear of the trough as the particle pile spread out with the increased impinging power of the 11.8 kg/m/s curtain.

At mass flow rates of 11.8 kg/m/s freefall transmittance was ~2-3% *lower* than that of the two-trough interrupted curtain. Figure 12 shows the increase in curtain transmissivity for both the 12” and 24” trough configuration, shown in blue, and the 12” and 36” stAIR configuration, shown in yellow. The increased transmissivity was due to the introduction

of the troughs 12” from the curtain origin. It was postulated that if the troughs had been introduced further from the curtain origin the transmissivity would decrease compared to a freefalling curtain at the same location.

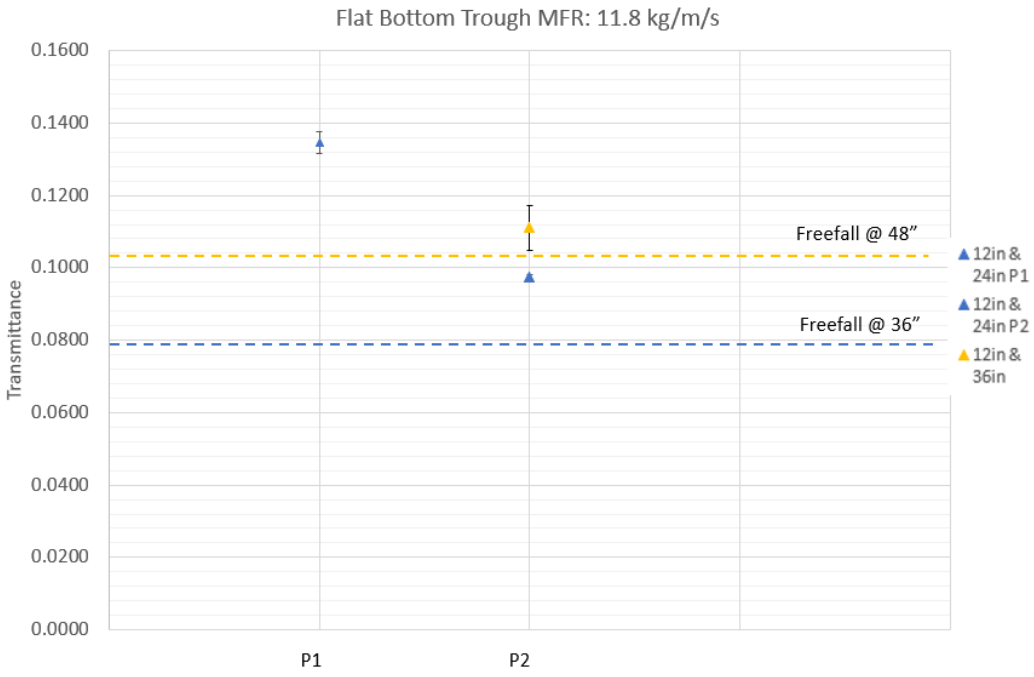

Figure 12: Transmissivity for two trough configuration at a mass flow rate of 11.8 kg/m/s

3.1.2.7 Multiple trough curtain behavior

The implementation of troughs induces horizontal momentum on the curtain leaving the trough. This behavior is compounded at the curtains interface at the second trough. The horizontal momentum was increased by the second trough causing an increase in particle bounce and curtain spread shown in Figure 13. Distances of 12” between troughs for both the flat bottom and 90-degree geometries resulted in less particle bounce than distances of 24”.

Figure 13: 2 stAIR tests at 4.1 kg/m/s. Inter stAIR distances of 4"(leftmost), 8"(center), and 12" (rightmost).

At mass flow rates of 9.8-11.8 kg/m/s, the horizontal momentum imparted by the trough was significantly larger than that of a 3.9-4.1 kg/m/s mass flow rate curtain. With an increase of horizontal curtain spread the catchment area of the second trough must be larger for a curtain with a higher mass flow rate. Figure 14 shows the curtain interface with the second trough at a 4.1 kg/m/s mass flow rate and a 9.8 kg/m/s mass flow rate. Given the same vertical positioning, the curtain is spread significantly higher in the 11.8 kg/m/s case. Three flat bottom troughs were positioned with 8” between them and tested at 9.8 kg/m/s and 4.1 kg/m/s. The profile of the curtains in Figure 14 shows the curtain behavior at 4.1 kg/m/s was favorable while the curtain flowing at 9.8 kg/m/s had a significant amount of forward spread and particle bounce. It was postulated that with a larger trough catchment area the curtain could be

(1) *(2)*

Figure 14: Particle Bounce over 3 troughs. (1) Particle flow over 3 troughs at 4.1 kg/m/s. (2) Particle flow over 3 troughs at 9.8 kg/m/s. Inter trough distances of 8".

caught at mass flow rates ~10 kg/m/s. The hybrid trough was designed based on this hypothesis which resulted in the best performing trough geometry. Constraints on the bench

scale test stand limited the number of hybrid troughs that could be tested in series to one.

3.1.3 Bench Scale Conclusion

Tests were conducted with four trough geometries to determine the optimal vertical location with respect to the curtain origin, horizontal position with respect to the curtain impingement on the trough geometry, and orientation of the angle iron troughs. These permutations were considered at slot depths of ¼" and ½" corresponding to mass flow rates of 3.9-4.1 kg/m/s and 9.8-11.8 kg/m/s respectively. Multiple troughs configurations with lower inter-trough vertical spacing were shown to have the least transmissive curtain and

least particle bounce when compared to trough configurations with larger inter-trough distances. High mass flow rates create the possibility to bypass the second trough due to increased horizontal translation which can be solved by using a trough geometry with a larger catchment area.

The hybrid trough geometry resulted in the least transmissive curtain when compared to the 90-degree, 120-degree, and flat bottom trough geometries. With a single horizontal position and orientation, it was found that curtain transmissivity decreased with increasing vertical distance from 12”, 24”, and 36” from the curtain origin with a maximum decrease in transmissivity of 25% when compared to freefall at a mass flow rate of 3.9-4.1 kg/m/s. The hybrid trough geometry also featured the largest acceptance area decreasing the probability of the curtain missing the trough due to wind effects and was determined to have the least amount particle bounce. With the reduced curtain transmissivity achieved by using the hybrid trough StAIR design, the particle curtain has the potential to become more absorptive increasing the energy imparted on the particles by concentrated solar flux. The design was implemented into the 1 MW_{th} particle receiver to test this hypothesis.

CHAPTER 4

On-Sun Testing

On-sun receiver testing was conducted with a 1 MW_{th} falling particle receiver at the National Solar Test Facility starting late July 2020. Tests characterizing a series of receiver modifications with varying ambient conditions such as wind and ambient temperature are ongoing.

3.2.1 Method

3.2.1.1 Receiver Configuration and Measurement

Testing on the prototype 1 MW_{th} falling particle receiver at the NSTTF, Figure 15, has been ongoing since its initial construction in 2015. The test apparatus is composed of a 3x3 meter cavity receiver with a 1x1 meter north-facing aperture, an "Olds" skrew elevator, a top hopper above the receiver, and a bottom hopper which runs from the receiver to the bottom of the particle elevator. A slide gate at the bottom of the top hopper is controlled via a linear actuator. The actuator is advanced and retracted to open and close a slot out of which the particle curtain is created. A larger slot opening is associated with a larger particle mass flow rate and vice versa. The curtain falls from the slide gate through an opening in the top of the receiver to be irradiated by the incident solar flux and gathered in the bottom hopper.

The top hopper rests on 4 load cells which are summed to determine the weight of particles above the receiver. To measure the mass flow rate of the particles falling through the receiver, the Olds elevator is shut off stopping the flow of particles into the top hopper.

The particles continue to flow out of the slide gate reducing the weight of the top hopper allowing for the

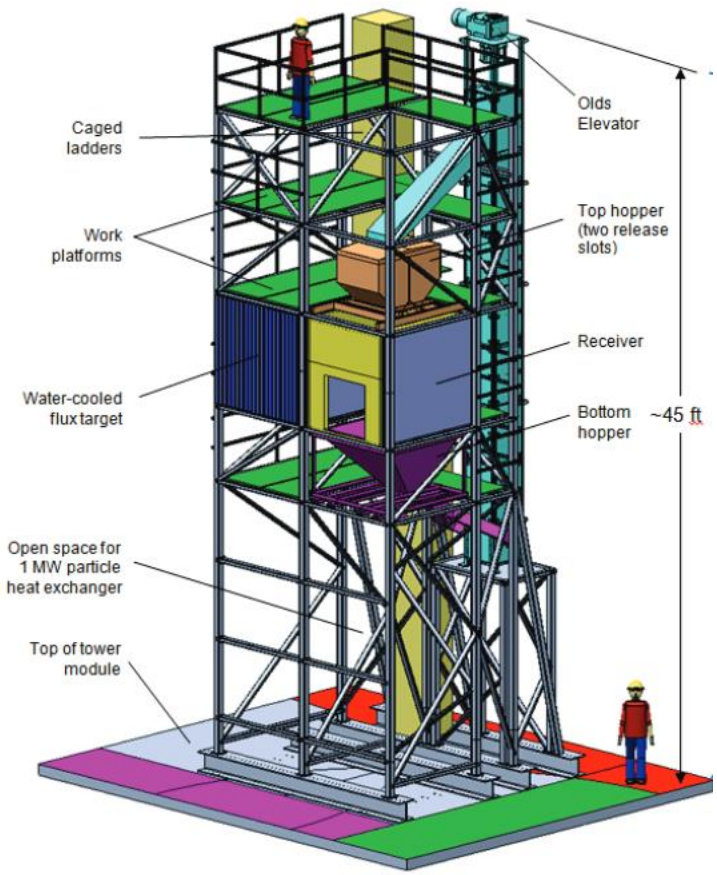

Figure 15: Schematic of the 1 MW falling particle receiver prototype system [17]

measurement of the mass flow through the receiver. A running average of the change in mass over a given sample period is taken on the FPRs DAQ and control system.

To measure the solar power incident on the particle curtain through the receiver aperture, the heliostat beam is positioned on a water-cooled calibration panel beside the receiver. A Kendall radiometer is mounted at the center of the calibration target to measure the peak flux at the center of the beam. Using the peak flux value, a LabVIEW program determines the power for a given aperture area, in this case, 1x1 meter. The program averages the pixel

intensity surrounding the Kendall on the uniformly colored flux target calibration panel. This pixel intensity is then assigned the peak flux value with pixels of decreasing intensity being assigned lower flux values based on a linear correlation. These flux values are then summed to determine the power over a given area.

Receiver outlet temperatures are determined using 5 funnels positioned below the receiver aperture above the top hopper. Each funnel directs particles to flow over thermocouples positioned at its base. The funnels ensure the thermocouples are submersed in particles preventing the measurement of ambient air in the receiver. The funnel temperatures are averaged to determine the particle outlet temperature of the receiver. Five thermocouples positioned above the slide gate at the bottom of the top hopper are averaged to determine the receiver inlet temperature.

3.2.1.2 Testing Goals

Brantley, Reid et al had conducted simulations for a reduced volume receiver and trough design which yielded higher thermal efficiencies when compared with the unmodified, freefalling, receiver design. [18] Modifications were made to the receiver to accommodate both designs to validate the simulated results and determine the impacts of environmental conditions such as wind and ambient temperature. The simulation had shown that at the 1 MW scale the trough design would not have a measurable impact on the receiver's efficiency. A simplified test matrix is outlined in

Table 1: A simplified test matrix for the 2020 on-sun test campaign [19]

Feature	Conditions	Goal
Reduced volume receiver (RVR)	Up to 700 °C particle temperature; 500 – 1000 kW/m^2; 5 – 10 kg/s particle flow	Measure the impact of reduced receiver-cavity volume on thermal efficiency; validate model
Multistage release	Up to 700 °C particle temperature; 500 – 1000 kW/m^2; 5 – 10 kg/s particle flow	Measure the impact of catch-and-release devices on backwall temperatures and thermal efficiency; validate model

Temperature control	Perturb irradiance by up to 50% by adjusting the number of heliostats	Use closed-loop feedback to maintain particle temperatures within ±10°C of setpoint temperature using slide-gate-controlled particle mass flow
Additional wind characterization	Use five additional ultrasonic wind anemometers around the receiver	Collect wind data to understand wind perturbations and impact on receiver efficiency

In this chapter results associated with the implementation of the trough design are outlined. Each trough configuration was tested with the reduced volume receiver.

3.2.1.3 Bracket Design

Implementing the trough design in the existing falling particle receiver required the analysis and construction of adjustable brackets shown in Figure 16. The brackets would need to carry the weight of 3 troughs full of particles and adjust vertically and horizontally inside the receiver. The maximum temperature measured in the receiver in previous tests was close to 900°C limiting the material selection to 304 stainless steel.

Vertical brackets were designed to be pinned to the east and west walls of the receiver. The brackets were made from two 60”x 2”x2” square tubes adjoined with four 20”x 2”x2” angle irons. The angle irons were pinned into the receiver walls through slotted holes to allow for thermal expansion. Each vertical tube was machined with 24 keyhole slots for the attachment of a horizontal plate. The keyholes on the northern tube included a slide to accommodate the axial growth.

A horizontal plate was designed with 4 pins, 2 pins on the north and south sides, to mount into the keyholes on the vertical brackets. The horizontal plates could be adjusted up and down inside the receiver using different vertical keyholes. The plate was machined with 20, 45°, keyholes. A 45° keyhole was implemented to prevent the rotation of the trough under load.

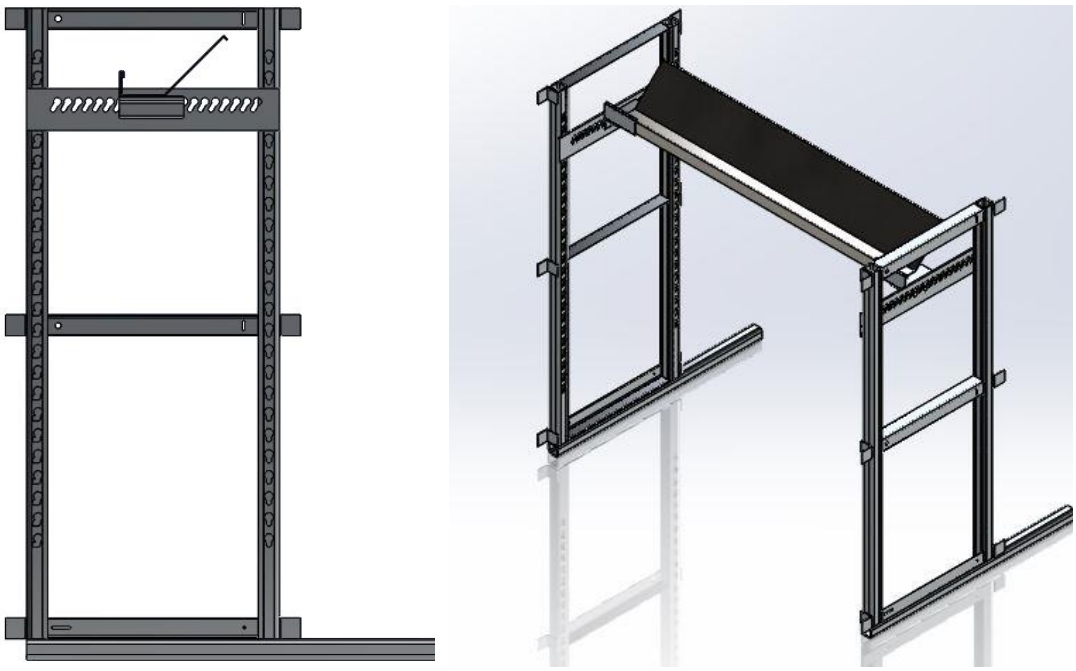

(1) (2)

Figure 16: (1)North facing view of trough mounting structure. The hybrid trough geometry can be seen resting on the bracket above the horizontal plate. (2)An isometric view of a single hybrid trough mounted in the

Brackets were designed with 2 pins to fit into the 45° keyholes. The brackets could be translated along the keyholes to adjust the position of the troughs in the north and south direction. The brackets attach to the trough with a lip that fits around the troughs leading edge. This lip prevents the rotation of the trough with the vertical load being taken by the horizontal portion.

FEA simulations were conducted on the structure using a prescribed trough weight of 45 kg. The maximum stress in each component was determined and compared to the yield strength 304 SS de-rated at 900 ° C. Multiple iterations were considered to ensure the structure could support the load under temperature, thermally expand, and maintain minimal strain values to allow for continued adjustability without binding.

3.2.1.4 Cold Flow Testing

With the brackets in place, multiple trough positions were considered. Due to the short distance between the slide gate and the front of the receiver, a three-trough configuration was not tested. As troughs translate the curtain forward toward the aperture, particle attrition and wind effects on the curtain increase. A two-trough configuration brought the curtain within a foot of the aperture. A third trough would translate the particle curtain out of the receiver.

Three, two trough configurations were considered with troughs abutting one other at the top of the receiver, troughs abutting each other in the center of the receiver, and with ~18” gap between the troughs shown in Figure 17. The two troughs were moved up and down in the receiver to determine an ideal location based on particle bounce. The two trough configuration is seen in Figure 17(1) was chosen for on-sun testing.

(1) *(2)* *(3)*

Figure 17: Two trough configuration in Falling Particle Receiver. (1) 2 troughs abutted at the topmost position inside the receiver. (2) two troughs abutted in the center of the receiver. (3) two troughs with an 18" gap between them.

One trough configuration was chosen for on-sun testing due to the poor freefalling curtain behavior. Thermal expansion causes warping to occur in the chute at the top of the receiver which induced a wavy uneven curtain shown in

(1)

(2)

Figure 18

(1). The trough catch and release design created a more stable homogenous curtain seen in

Figure 18(2).

Figure 18 Comparison between freefalling curtain (1) and a single trough interrupted curtain (2).

3.2.1.5 Test Operation

Receiver efficiency was measured with varying inlet temperature, irradiance, and trough configurations. A simplified list of these parameters is shown in Table 2. The goal of the test campaign was to gather data with varying receiver configurations with a range of environmental conditions. This section will focus on the effects of the trough configuration on thermal efficiency.

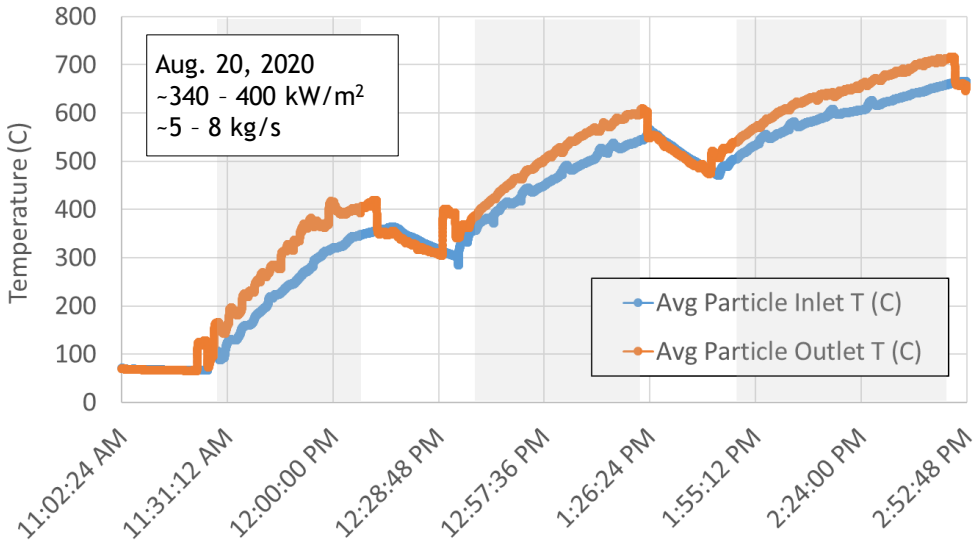

Figure 19: shows the particle inlet and outlet temperature for a given test day. [19]

The highlighted regions below indicated time in which the particles falling through the receiver were heated with solar flux. The orange line represents the receiver outlet temperature which can be seen to exceed the receiver inlet temperature in blue. A mass flow rate between ~5-8 kg/m/s was used with an incident solar irradiance of ~340-400 kW/m^2. The concentrated sunlight was moved on and off the receiver to take incident power measurements and to let the particles cool to maintain a given particle inlet

temperature as there was no particle heat sink in the FPR system. Particle flow into the top hopper was stopped periodically to measure the mass flow rate of the particle curtain resulting in oscillations in particle inlet temperature shown on the blue line.

A given test day would begin with a ramp in particle temperature from ambient to a desired particle inlet temperature. Measurements with varying irradiance were taken while keeping the particle mass flow rate, and particle inlet temperature relatively constant allowing for the isolation irradiance as the dependent variable. The particle mass flow rate was then changed to conduct the same set of irradiance tests. The majority of the tests were taken with a 400-600°C particle inlet temperature to simulate the operation temperatures proposed for G3P3-USA. Higher particle inlet temperatures have been associated with greater thermal losses. [20].

3.2.2 Theory

To calculate the receiver thermal efficiency, η_{th}, the ratio of the power absorbed by the particles, Q_{abs} (W), and the total solar power through the receiver aperture, Q_{in}(W) was taken. The equation below describes the derivation of the receiver thermal efficiency.

$$\eta_{th} = \frac{Q_{abs}}{Q_{in}} = \frac{\dot{m}(h_{out} - h_{in})}{Q_{in}} = \frac{\dot{m}\int_{T_{in}}^{T_{out}} c_p(T)dT}{Q_{in}} = \frac{\dot{m}\left[113.2\left(T_{out}^{1.3093} - T_{in}^{1.3093}\right)\right]}{Q_{in}} \quad (2)$$

Where $\dot{m}$ is the mass flow rate (kg/s), h_{out} is the enthalpy of the particles exiting the receiver (J/kg), h_{in} is the enthalpy of the particle entering the receiver (J/kg), $c_p(T)$ is the temperature-dependent specific heat of the particles (J/kg·K), T_{in} is the temperature of the particles entering the receiver (K), and T_{out} is the temperature of the particles exiting the

receiver (K). The specific heat of the particles, CARBO HSP 40/70, is given by the following correlation.

$$c_p = 148.2T(K)^{0.3093} \qquad (3)$$

The particle mass flow rate, $\dot{m}$, and power incident through the receiver aperture, Qin, were measured discretely before and/or after a sample period while the receiver inlet and outlet temperatures were measured continuously at a rate of 1 Hz. Sample periods in which the receiver efficiency was calculated ranged from 40 seconds to 5 minutes. The particle inlet and outlet temperatures were averaged over the sample period to calculate receiver efficiency. Temporal thermocouple and uncertainty errors were propagated with each measurement to generate the total error.

The theoretical maximum receiver efficiency was calculated for 350-750°C particles using the following equation.

$$\eta_{th,\max} = \frac{\alpha Q_{in} - Q_{loss}}{Q_{in}} = \alpha - \frac{\varepsilon\sigma A\left(T_{p,ave}^4 - T_{amb}^4\right) + hA(T_{p,ave} - T_{amb})}{Q_{in}} = 1 - \frac{\sigma A\left(T_{p,ave}^4 - T_{amb}^4\right)}{Q_{in}} \qquad (4)$$

Where α is the curtain absorptance (=1 for an ideal case), ε is the emissivity (=0 for a cavity receiver), σ is the Stefan-Boltzmann constant ($5.67\text{x}10^{-8}$ W/m^2-K^4), A is the receiver aperture area (1 m^2), $T_{p,ave}$ is the average particle temperature (K), T_{amb} is the ambient temperature (K), and h is the falling particle convective heat transfer coefficient (=0 for theoretical maximum). [19]. The theoretical maximum efficiencies neglecting advective losses are plotted in Figure 20. The theoretical maximum efficiency helped verify the reliability of the measurement gathered.

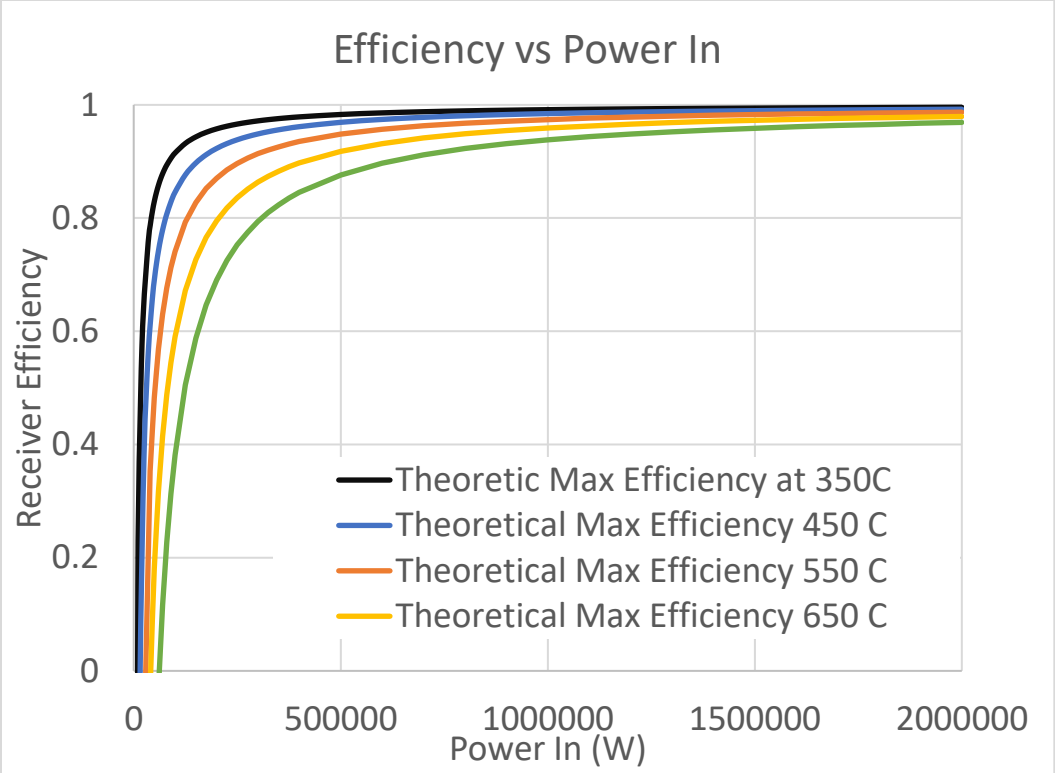

Figure 20: Maximum receiver efficiencies as a function of incident power at particle temperatures from 350C to 750C.

3.2.3 Results

Forest fires burning in the summer of 2020 created significant amounts of smoke which limited the maximum irradiance to ~800 kW/m^2 in the test campaign. Attenuation through atmospheric smoke/dust scatters the beam of concentrated sunlight onto the shielding surrounding the aperture causing damage. Higher irradiance results in higher receiver efficiencies shown in Figure 20. Testing conducted in 2018 using a freefalling curtain achieved higher efficiencies due to higher incident power.

Table 2 lists the calculated receiver efficiencies for a variety of tests conducted during the campaign. Efficiencies were measure as high as 85-90% for multiple one trough scenarios. Two trough configurations resulted in higher curtain spread biasing higher measured

receiver outlet temperature. This resulted in calculated efficiencies of over 100%. Current tests are correcting for this error with expected efficiencies of >80%.

Table 2: 2020 Test campaign results, [1]Wind direction 1-360 with 360 indicating north

Date	Irradiance (kW/m^2)	Mass Flow Rate (kg/s)	Tin (°C)	Tout (°C)	Thermal Efficiency	Ambient T (°C)	Wind Speed (m/s)	Wind Direction[1]	Number of StAIRs
8/17/2020	68	2.38	545	629	47%	31	3.2	251	2
8/17/2020	115	8.09	534	611	84%	31	4.4	159	2
8/18/2020	59	6.43	667	715	86%	28	2.8	170	2
8/18/2020	120	6.47	584	692	92%	30	1.8	325	2
8/20/2020	43	2.96	307	391	78%	30	1.0	304	2
8/20/2020	41	5.90	534	578	83%	32	1.8	219	2
8/20/2020	44	5.81	661	704	84%	32	0.9	304	2
8/20/2020	45	5.77	606	654	92%	33	2.6	288	2
8/21/2020	45	5.79	585	630	88%	28	5.2	348	1
8/21/2020	33	7.48	323	356	81%	29	1.8	273	1
8/21/2020	41	5.79	581	630	93%	30	2.9	331	1
9/4/2020	49	6.46	680	716	72%	27	2.1	214	1
9/4/2020	60	6.69	528	575	75%	28	3.7	239	1
9/4/2020	56	9.19	546	570	57%	28	1.9	282	1
9/4/2020	60	6.40	627	682	87%	29	1.9	237	1
9/18/2020	63	9.27	573	595	72%	21	2.9	242	1
9/18/2020	69	9.02	779	802	53%	22	2.9	296	1
9/18/2020	60	7.61	585	613	54%	22	3.3	221	1
9/18/2020	69	10.07	776	799	54%	22	2.7	261	1
9/18/2020	68	8.24	752	788	71%	23	3.9	256	1
9/18/2020	68	7.19	692	735	72%	23	1.3	272	1
9/18/2020	56	4.23	512	586	82%	23	2.2	204	1
9/18/2020	55	5.29	484	551	93%	23	2.5	237	1
9/22/2020	8	7.35	438	442	58%	26	3.3	291	1
9/22/2020	16	7.35	428	440	74%	26	1.4	312	1
9/22/2020	24	7.35	413	431	75%	26	4.1	345	1
9/22/2020	31	7.35	410	438	88%	26	4.2	285	1
9/22/2020	42	7.35	432	469	91%	26	5.0	287	1
9/22/2020	53	7.01	446	497	94%	26	4.0	303	1
9/22/2020	68	7.25	435	502	99%	27	4.3	292	1
9/24/2020	9	3.89	490	490	54%	27	3.3	287	1
9/24/2020	35	4.57	457	457	63%	27	3.3	329	1
9/24/2020	18	3.88	477	477	63%	27	2.9	290	1
9/24/2020	27	3.88	465	504	73%	27	5.4	303	1
9/24/2020	50	4.30	489	489	83%	27	3.4	281	1
9/24/2020	60	4.67	482	482	85%	27	5.7	285	1
9/24/2020	47	4.67	459	459	88%	27	2.8	293	1
9/24/2020	68	4.67	511	511	93%	27	4.4	277	1
9/24/2020	66	4.67	511	511	93%	27	4.4	275	1
9/25/2020	9	7.46	478	481	27%	28	4.7	330	1
9/25/2020	18	7.90	466	477	66%	28	3.9	311	1
9/25/2020	48	7.39	473	505	79%	28	5.7	303	1
9/25/2020	36	7.39	473	499	73%	28	5.5	296	1
9/25/2020	27	7.90	460	478	75%	28	4.4	321	1
9/25/2020	71	6.85	548	607	83%	28	7.8	303	1

Date	Irradiance (kW/m^2)	Mass Flow Rate (kg/s)	Tin (°C)	Tout (°C)	Thermal Efficiency	Ambient T (°C)	Wind Speed (m/s)	Wind Direction[1]	Number of StAIRs
9/25/2020	71	7.31	515	576	91%	28	5.9	287	1
9/25/2020	62	7.39	479	534	83%	28	3.4	320	1

Receiver efficiency is highly dependent on the mass flow rate and particle inlet temperature. High particle mass flow rates are associated with higher receiver efficiencies due to the increased opacity and thus absorptance of the particle curtain. Inlet temperature informs what

radiative and advective thermal losses to expect as the particle fall through the receiver. At higher inlet temperatures the thermal losses increase as a ratio of power absorbed by the particles. Particle inlet temperature was isolated in

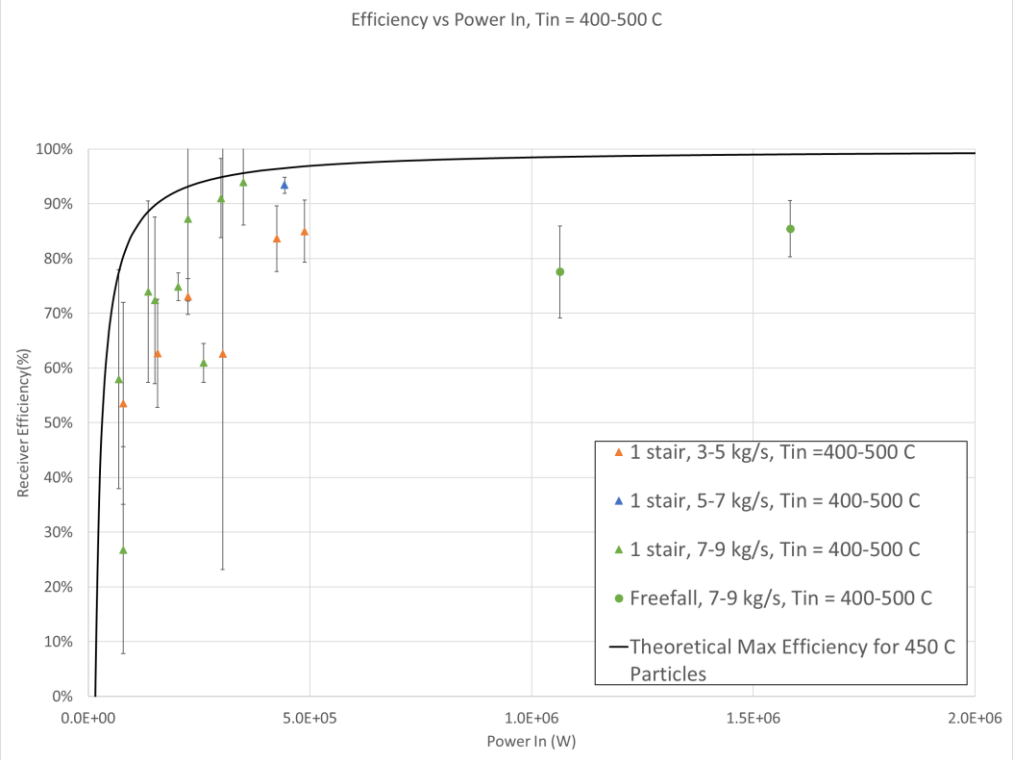

Figure 22 which shows the theoretical maximum receiver efficiency for particles at 450°C compared to the calculated receiver efficiency. Inferring a trend line for the one stAIR configuration

can give insight into the increased efficiency compared to freefalling cases at higher incident powers. At incident powers less

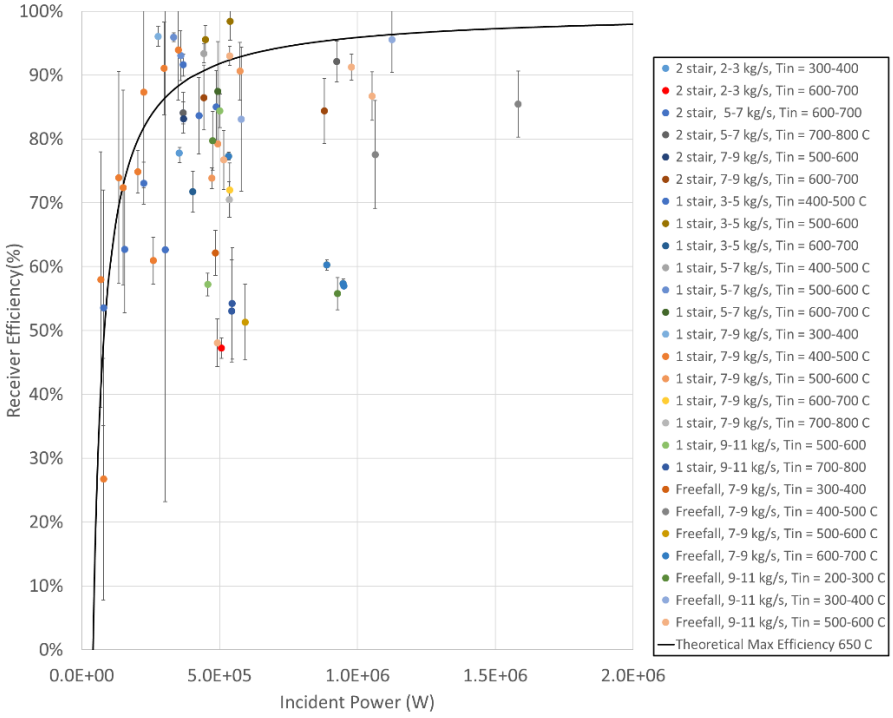

Figure 21: Receiver efficiency as a function of power into the receiver aperture including freefalling, one trough, and two trough cases.

The receiver back wall temperature was recorded during each receiver efficiency test. In previous tests conducted in 2018 using a freefalling curtain the back wall had been damaged during high irradiance, low mass flow rate testing indicating temperatures exceeding the refractory materials temperature limit of around 1000°C. [21] During the 2020 on-sun test campaign back wall temperatures never exceeded the limit of the refractory material. Figure 23 shows the backwall, receiver inlet, and receiver outlet temperatures for a test day in which flux values up to 1000 suns resulting 784 kW of incident power was focused on the receiver. Mass flow rates varied from 3 to 8 kg/m/s throughout the test day with a two-trough stAIR configuration. Despite the low mass flow

rate and high incident power, the receiver backwall temperature never exceeded the 1000°C limit of the refractory material suggesting the particle curtain opacity and thus absorptivity prevented the concentrated sunlight from passing though the curtain to the receiver's back wall.

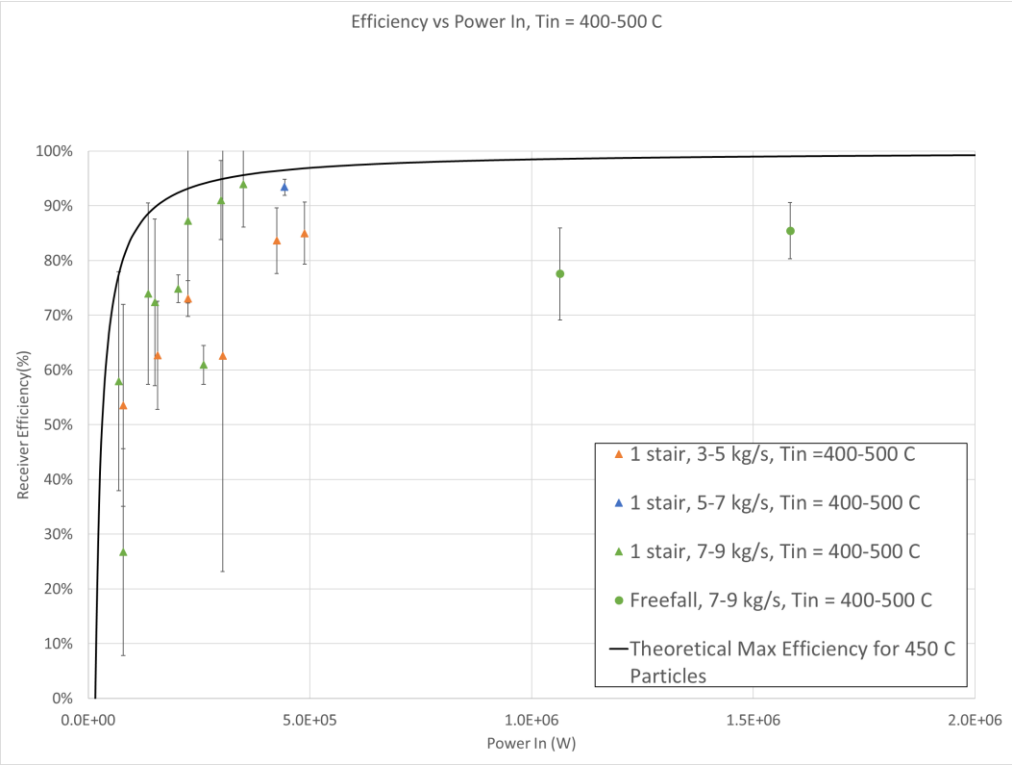

Figure 22: Receiver efficiency with one stAIR, circle marker, and freefall, triangle marker, configurations. Mass flow rates between 3-5 kg/s are shown in orange, 5-7 in blue, and 7-9 in green.

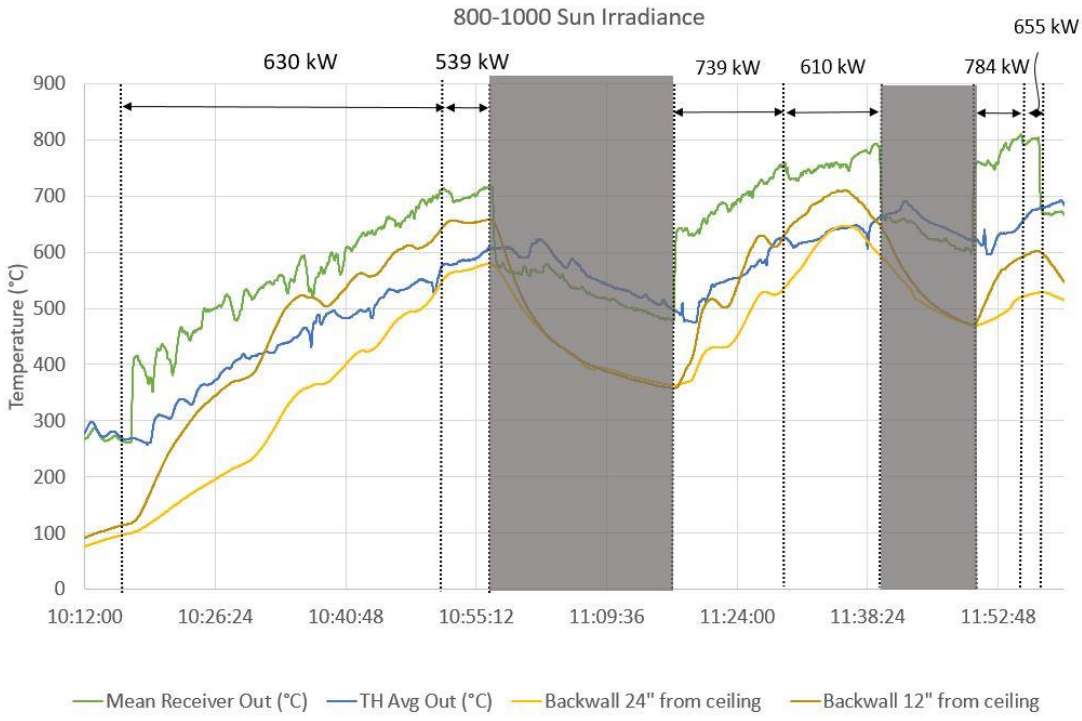

Figure 23: High irradiance test day highlighting receiver back wall temperatures

CHAPTER 5

Future Work

On-Sun receiver testing in this campaign is ongoing with future experiments supplying more data for the 2-trough and freefall receiver configurations with and without the reduced receiver volume. The increased number of data points will provide insight into the impact of environmental conditions such as wind and ambient temperature.

Additional testing for the FPR includes particle dust sampling to determine how dust created from particle abrasion impacts the environment, beam attenuation, and its impact on receiver efficiency. A freefalling curtain with the reduced receiver volume will tested and compared to the efficiencies measured with the StAIR design. With continued testing and clearing skies, the conditions present in the 2018 test campaign can be replicated for the determination of the receiver modification effect on thermal efficiency.

A method of controlling the particle outlet temperature is currently being evaluated using a PID controlled slide. The slide gate controls the mass flow rate through the receiver with higher mass flow rates yielding low receiver outlet temperatures and vice versa.

CONCLUSION

Multistage release structures have the potential to increase curtain stability, curtain opacity, and thus thermal efficiency in falling particle receiver systems. A Staggered Angle Iron Receiver design was considered using a bench-scale test stand to determine the structure's effect on curtain transmissivity and particle bounce while on-sun receiver testing was used to determine the design's effect on thermal efficiency.

Through the testing of four trough geometries at varying vertical locations, horizontal positions, and orientations, an optimal, hybrid trough, geometry was found that resulted in an up to 14% decrease in curtain transmissivity when compared with a freefalling curtain. One and two trough configurations were implemented in a preexisting 1 MW_{th} falling particle receiver for on-sun testing. Receivers efficiencies were calculated with irradiances from 100 to 1000 suns, mass flow rates from 2 to 11 kg/s, and particle inlet temperatures ranging from 300°C-800°C. Theoretical maximum receiver efficiencies were calculated for particle temperatures from 350°C to 750°C neglecting advective losses to validate the calculated efficiencies. Maximum one trough, two trough, and freefall receiver efficiencies ranged from 85%-96% with a peak efficiency of 86% achieved for the 2020 test campaign for a one trough configuration with a mass flow rate of 5-7 kg/s and a particle inlet temperature of 500°C-600°C at an incident power of 334000W. A previous test campaign conducted in 2018 achieved a freefall efficiency of 96% with a mass flow rate of 9-11 kg/s, an inlet temperature of 300°C-400°C, and an incident power of 1125600 W. Using trends in the one and two trough data it is assumed that at similar conditions the receiver efficiency could surpass receiver efficiencies utilizing a freefalling curtain.

ACKNOWLEDGEMENTS

This work was funded in part or whole by the U.S. Department of Energy Solar Energy Technologies Office under Award Number 34211. This report was prepared as an account of work sponsored by an agency of the United States Government. Neither the United States Government nor any agency thereof, nor any of their employees, makes any warranty, express or implied, or assumes any legal liability or responsibility for the accuracy, completeness, or usefulness of any information, apparatus, product, or process disclosed, or represents that its use would not infringe privately owned rights. References herein to any specific commercial product, process, or service by trade name, trademark, manufacturer, or otherwise does not necessarily constitute or imply its endorsement, recommendation, or favoring by the United States Government or any agency thereof. The views and opinions of the authors expressed herein do not necessarily state or reflect those of the United States Government or any agency thereof.

Sandia National Laboratories is a multimission laboratory managed and operated by National Technology and Engineering Solutions of Sandia, LLC., a wholly owned subsidiary of Honeywell International, Inc., for the U.S. Department of Energy's National Nuclear Security Administration under contract DE-NA0003525.

REFERENCES

[1] C. Ho, "Advances in Central Receiver for Concentrating Solar Applications," *Solar Energy,* vol. 152, pp. 38-56, 2017.

[2] "Concentrating Solar Power Projects," March 2017. [Online]. Available: https://solarpaces.nrel.gov/planta-solar-10.

[3] "Sandia Labs Shares Major Solar Success with Industrial Consortium," 1996. [Online]. Available: http://www.sandia.gov/media/solar11.htm.

[4] R. W. Bradshaw and D. E. Meeker, "High-Temperature Stability of Ternary Nitrate Molten-Salts for Solar Thermal-Energy Systems," *Solar Energy Matter,* vol. 21, pp. 51-60, 1990.

[5] J. Hurby, R. Steeper, E. G.H and C. Crowe, "An Experimental adn Numerical Study of Flow and Convective Heat Transfer in a Freely Falling Curtain of Partilces," 1986. [Online]. Available: http://www.osti.gov/servlets/purl/1616232.

[6] K. Stahl, J. Griffin, B. Matson and R. Pettit, "Optical Characterization of a Solid Particle Solar Central Receiver Materials," 1986. [Online]. Available: https://www.osti.gov/servlets/purl/5829925.

[7] K. Kim, N. Seigel, G. Kolb, V. Rangaswamy and S. Moujaes, "A Study of Solid Particle Flow Characterization in Solar Particle Receiver," *Solar Energy,* pp. 1784-1783, 2009.

[8] J. M. Christian, W. Kolb, J. Kelton and D. Ray, "Design and Evaluation of an On-Sun Prototype Falling Particle Cavity Receiver," *ES Fuel Cell,* 2014.

[9] C. Ho, J. Christian, J. Yellowhair, S. Jeter, M. Golob, C. Nguyen, K. Repole, S. Abdel-Khalik, N. Siegel, H. Al-Ansary, A. El-Leathy and B. Gobereit, "Highlights of the High-Temperature Falling Particle Receiver Project: 2012-2016," in *AIP Conference Proceedings*, 2017.

[10] T. Lee, S. Lim, S. Shin, D. Sadowski, S. Abdel-Khalik, S. Jeter and H. Al-Ansary, "Numerical Simulation of a Particulate Flow in Interconnected Porous Media for Central Particle-Heating Receiver Applications," *Solar Energy,* vol. 113, pp. 14-24, 2015.

[11] M. Ebert, J. Rheinlander, B. Schlogl-Knothe, S. Schmitz, M. Sibum, R. Uhlig and R. Buck, "Operational Experience of a Centrifugal Particle Receiver Prototype," in *AIP*, 2019.

[12] J. Kim, A. Kumar, W. Gardner and W. Lipinski, "Experimental Investigation of a Novel MultiStage Falling Particle Receiver," in *AIP*, 2019.

[13] K. Kim, S. Moujaesb and G. Kolb, "Experimental and Simulation Study on Wind Affected Particle Flow in a Solar Receiver," *Solar Energy,* no. 84, pp. 263-70, 2010.

[14] M. Mehos, C. Turchi, J. Vidal, M. Wagner, Z. Ma and M. Mehos, "Concentrating Solar Power Gen3 Demonstration Roadmap," NREL, 2017.

[15] "CSP Projects Around the World," SolarPACES, 2020. [Online]. Available: https://www.solarpaces.org/csp-technologies/csp-projects-around-the-world/.

[16] C. K. Ho, M. Carlson, P. Garg and P. Kumar, *Technoeconomic Analysis of Alternative Solarized s-CO2 Brayton Cycle Configurations,* vol. 138, 2016.

[17] C. K. Ho, J. Christian, J. Yellowhair, S. Jeter, M. Golob, C. Nguyen, K. Repole, S. Abdel-Khalik, N. Siegel, H. Al-Ansary, A. El-Leathy and B. Gobereit, "Highlights of the high-temperature falling particle receiver project: 2012 - 2016," in *AIP Conference Proceedings* , 2017.

[18] R. Shaeffer, B. Mills, L. Yue and C. K. Ho, "Evaluation of Performance Factors for a Multistage Falling Particle Receiver," in *ASME Energy Sustainability* , Virtual, 2020.

[19] C. Ho, N. Schroeder, H. Laubscher, L. Yue, B. Mills, R. Shaeffer, J. Christian and K. Albrecht, "Receiver Design and On-Sun Testing for G3P3-USA," in *SolarPACES*, 2020.

[20] B. Mills and C. Ho, "Simulations and Performance Evaluation of On-Sun Particle Reciever Tests," in *AIP*, 2019.

[21] "RSLE Boards - General Info," ZRCI Refractory Composites , 2019. [Online]. Available: http://www.zrci.com/material/rsle-57-board-2/.

[22] B. Gobereit, L. Amsbeck, R. Buck, R. Pitz-Paal and H. Muller-Steinhagen, "Assessment ofa Falling Solid Particle Receiver with Numerical Simulation," in *SolarPACES*, Marrakech, Marrocco, 2012.

[23] "Concetrating Solar Power: Energy from Mirrors, Energy Efficiency and Renewable Energy," March 2001. [Online]. Available: https://www.nrel.gov/docs/fy01osti/28751.

APPENDIX

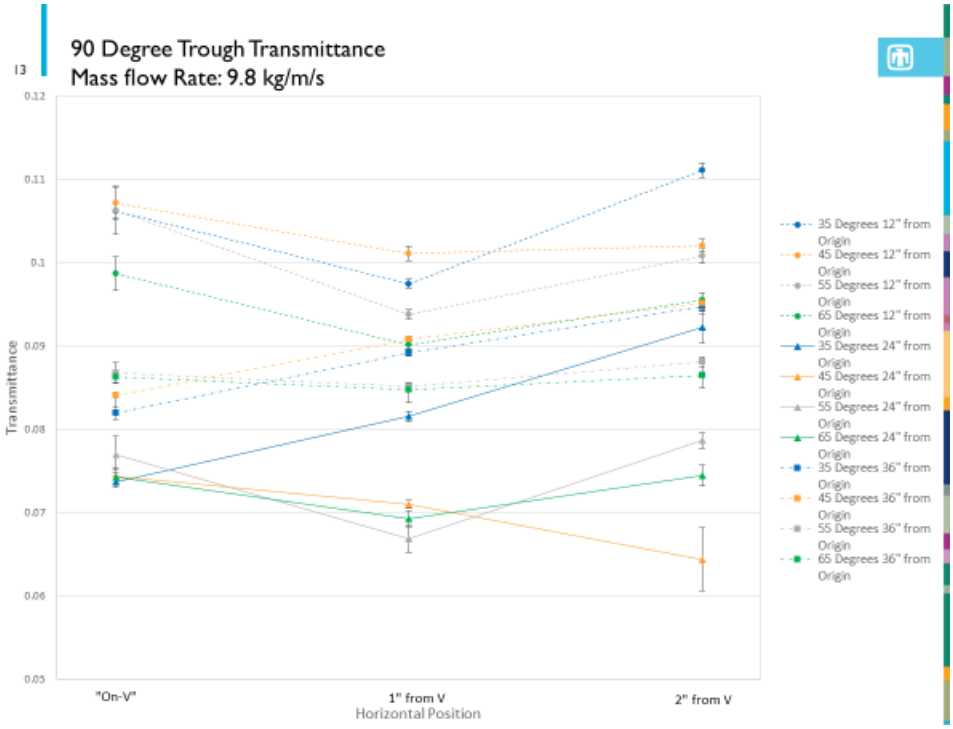
13
90 Degree Trough Transmittance
Mass flow Rate: 9.8 kg/m/s
Transmittance
0.12
0.11
0.1
0.09
0.08
0.07
0.06
0.05
"On-V"
1" from V
2" from V
Horizontal Position
35 Degrees 12" from Origin
45 Degrees 12" from Origin
55 Degrees 12" from Origin
65 Degrees 12" from Origin
35 Degrees 24" from Origin
45 Degrees 24" from Origin
55 Degrees 24" from Origin
65 Degrees 24" from Origin
35 Degrees 36" from Origin
45 Degrees 36" from Origin
55 Degrees 36" from Origin
65 Degrees 36" from Origin

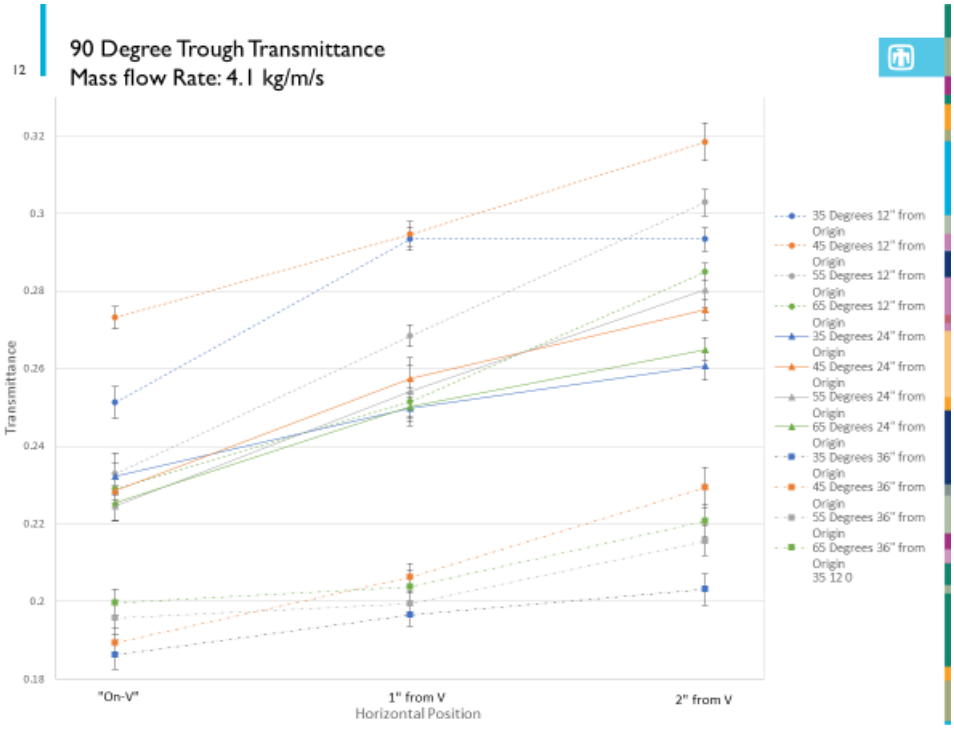
12
90 Degree Trough Transmittance
Mass flow Rate: 4.1 kg/m/s
Transmittance
0.32
0.3
0.28
0.26
0.24
0.22
0.2
0.18
"On-V"
1" from V
2" from V
Horizontal Position
35 Degrees 12" from Origin
45 Degrees 12" from Origin
55 Degrees 12" from Origin
65 Degrees 12" from Origin
35 Degrees 24" from Origin
45 Degrees 24" from Origin
55 Degrees 24" from Origin
65 Degrees 24" from Origin
35 Degrees 36" from Origin
45 Degrees 36" from Origin
55 Degrees 36" from Origin
65 Degrees 36" from Origin
35 12 0

17

120 Degree Trough
Mass Flow Rate: 4.1 kg/m/s

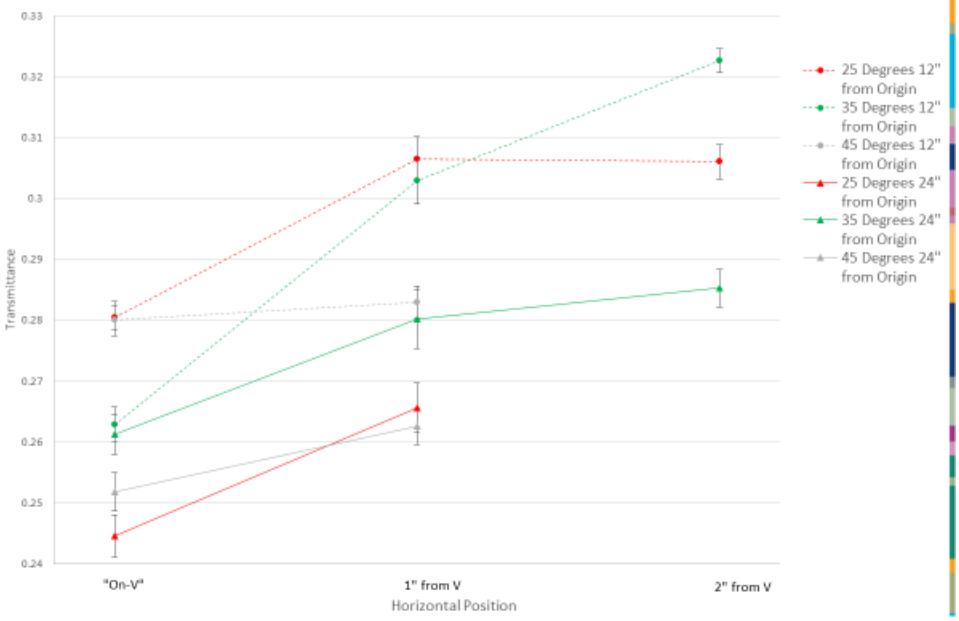

18

120 Degree Trough
Mass Flow Rate: 9.8 kg/m/s

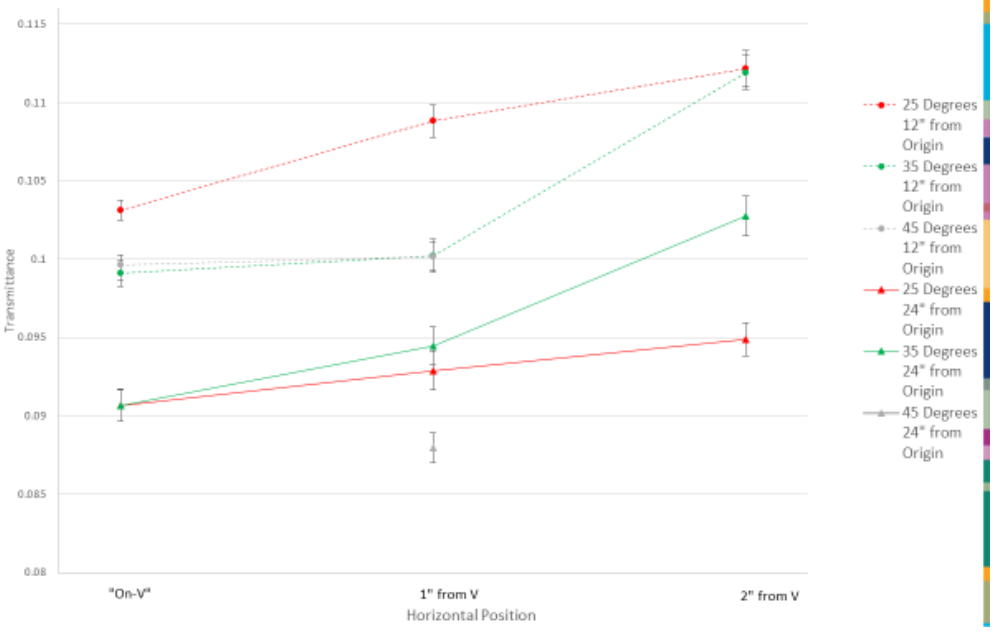

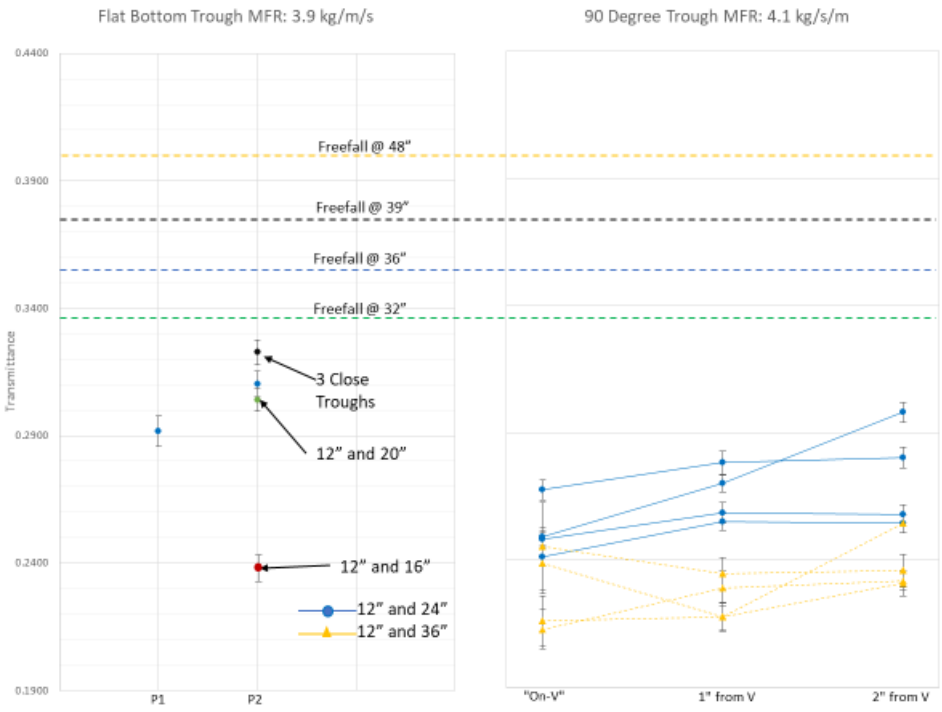
Flat Bottom Trough MFR: 3.9 kg/m/s
90 Degree Trough MFR: 4.1 kg/s/m
Freefall @ 48"
Freefall @ 39"
Freefall @ 36"
Freefall @ 32"
3 Close Troughs
12" and 20"
12" and 16"
12" and 24"
12" and 36"
Transmittance
P1
P2
"On-V"
1" from V
2" from V

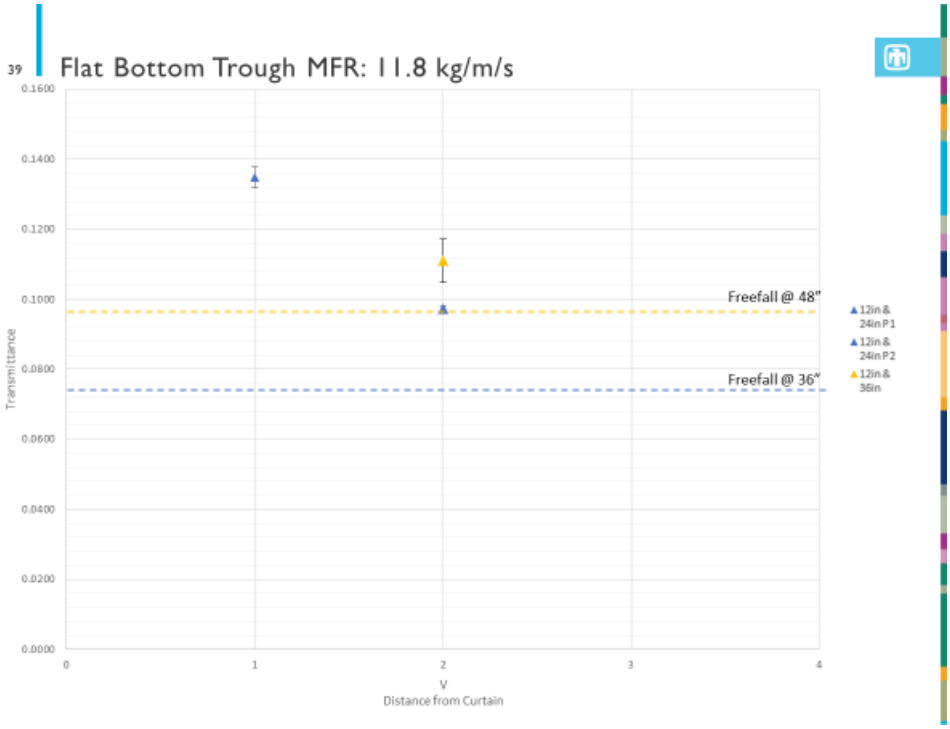
39
Flat Bottom Trough MFR: 11.8 kg/m/s
Freefall @ 48"
Freefall @ 36"
Transmittance
V
Distance from Curtain
12in & 24in P1
12in & 24in P2
12in & 36in

48

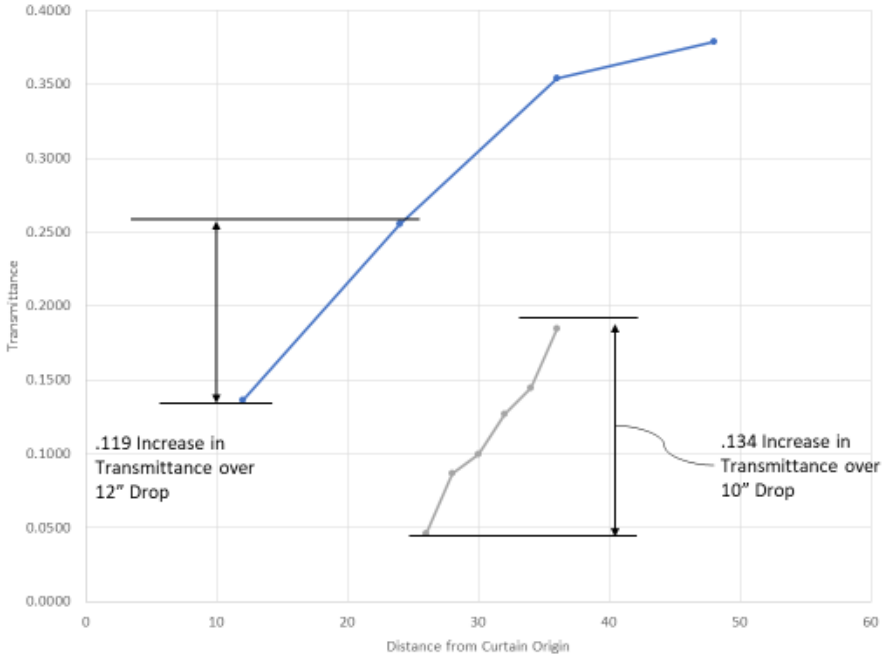
0.4000
0.3500
0.3000
0.2500
0.2000
0.1500
0.1000
0.0500
0.0000
Transmittance
0
10
20
30
40
50
60
Distance from Curtain Origin
.119 Increase in Transmittance over 12" Drop
.134 Increase in Transmittance over 10" Drop
Freefall
After 12in Step
After 24in step

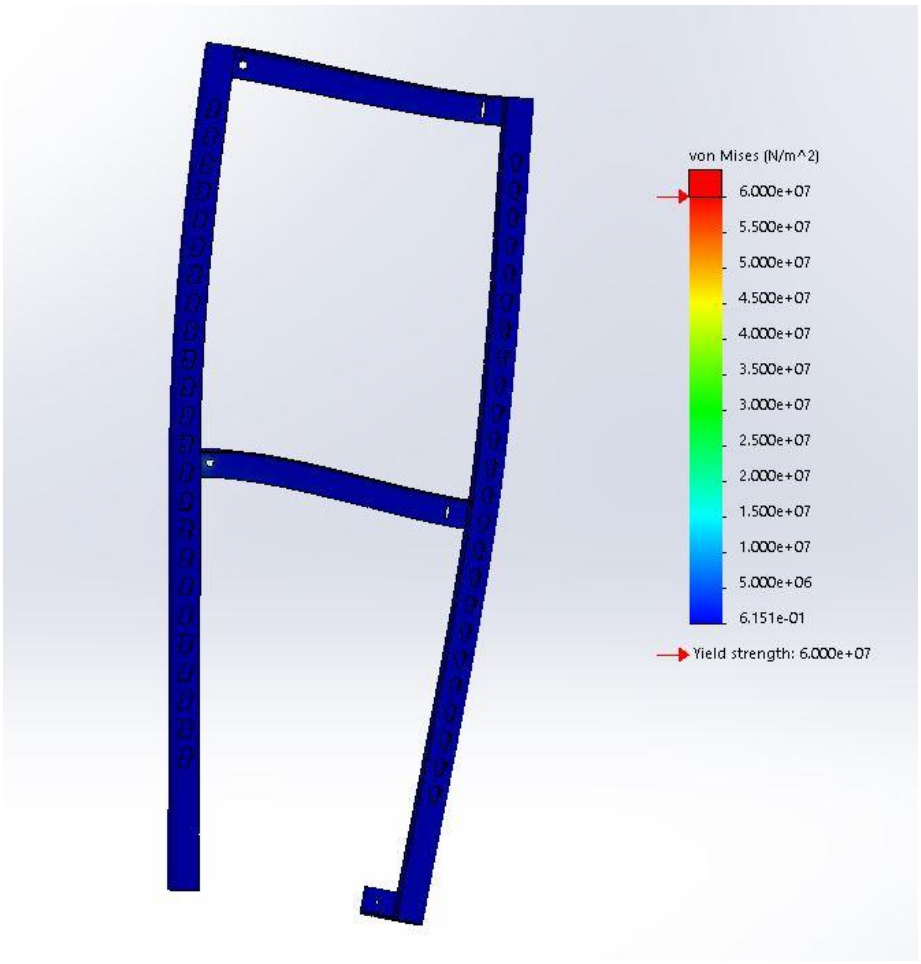
von Mises (N/m^2)
6.000e+07
5.500e+07
5.000e+07
4.500e+07
4.000e+07
3.500e+07
3.000e+07
2.500e+07
2.000e+07
1.500e+07
1.000e+07
5.000e+06
6.151e-01
Yield strength: 6.000e+07

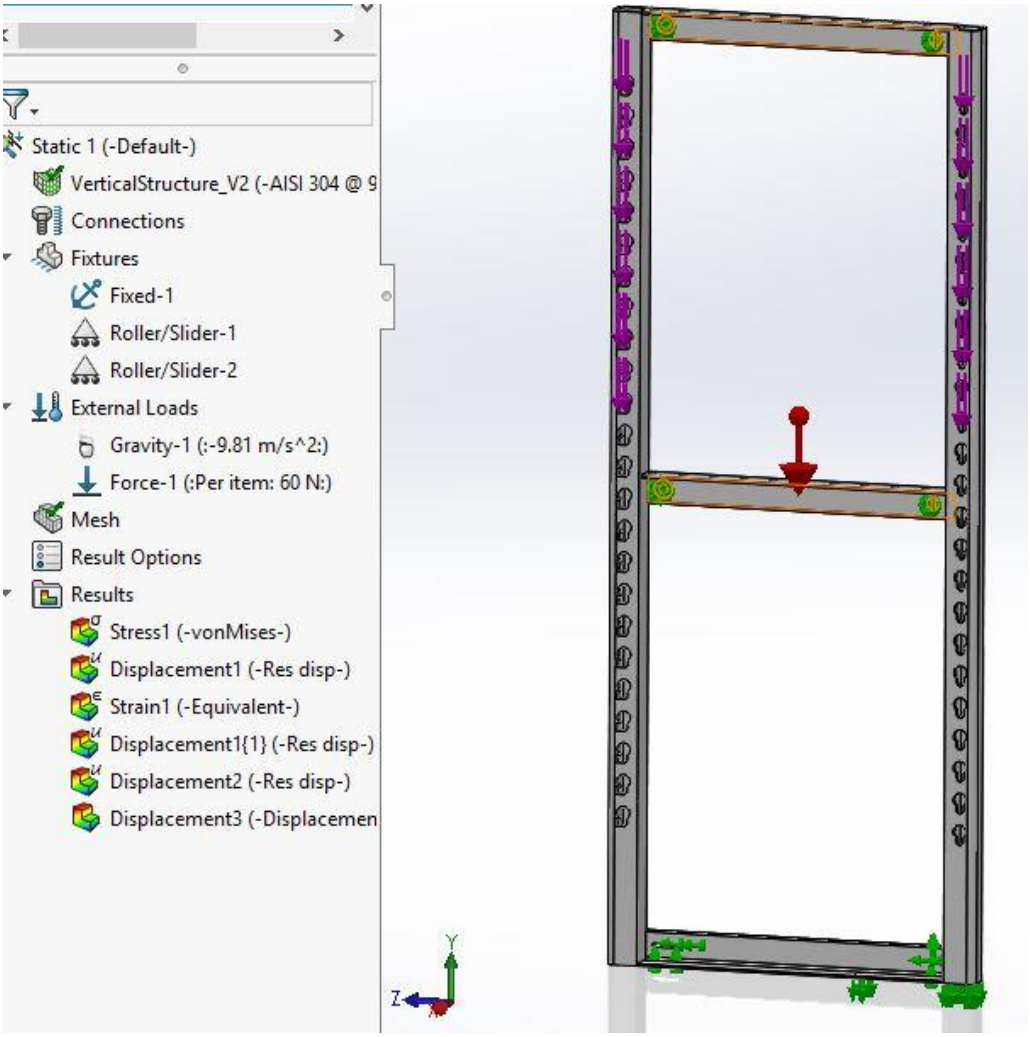
Static 1 (-Default-)
VerticalStructure_V2 (-AISI 304 @ 9
Connections
Fixtures
Fixed-1
Roller/Slider-1
Roller/Slider-2
External Loads
Gravity-1 (:-9.81 m/s^2:)
Force-1 (:Per item: 60 N:)
Mesh
Result Options
Results
Stress1 (-vonMises-)
Displacement1 (-Res disp-)
Strain1 (-Equivalent-)
Displacement1{1} (-Res disp-)
Displacement2 (-Res disp-)
Displacement3 (-Displacemen
Y
Z

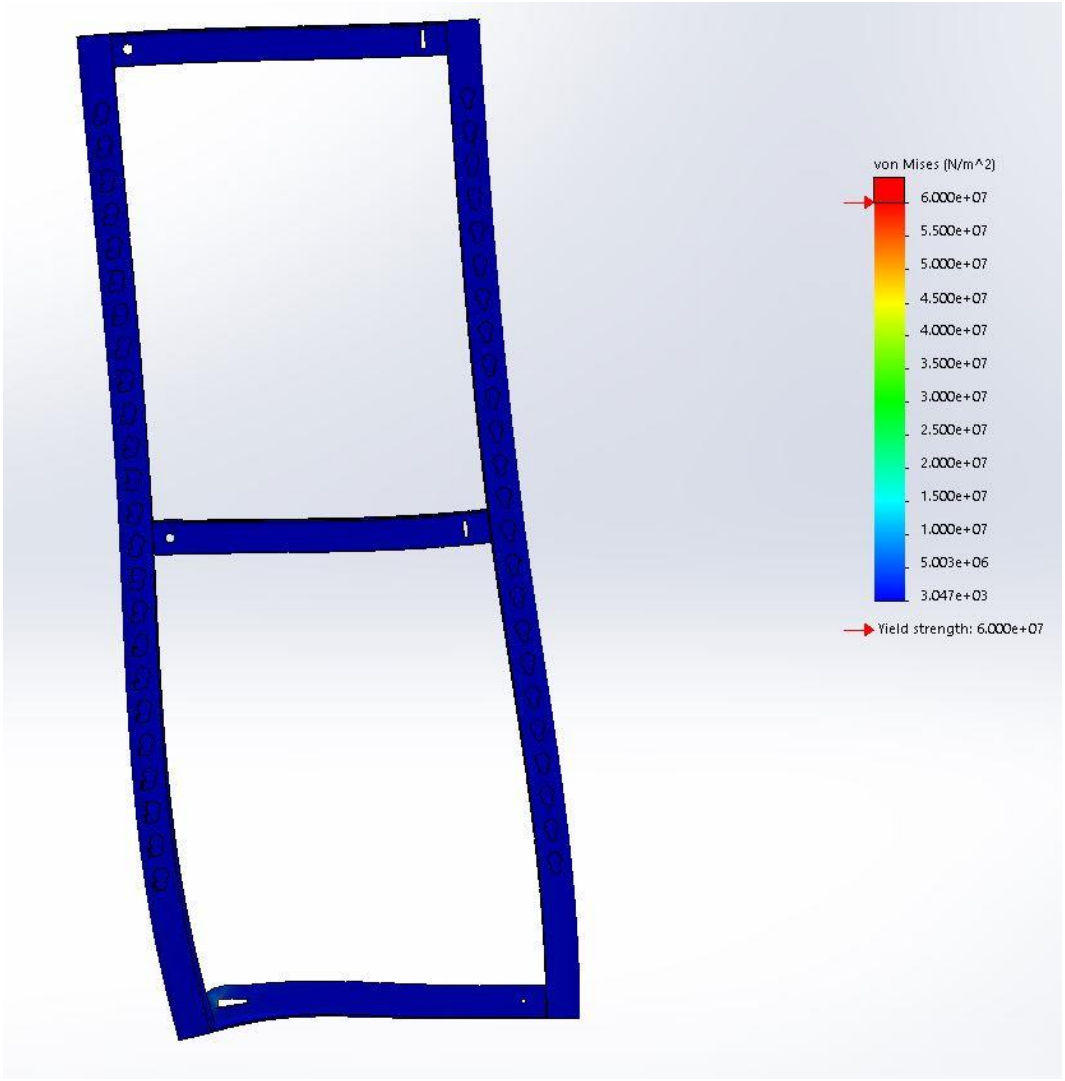
von Mises (N/m^2)
6.000e+07
5.500e+07
5.000e+07
4.500e+07
4.000e+07
3.500e+07
3.000e+07
2.500e+07
2.000e+07
1.500e+07
1.000e+07
5.003e+06
3.047e+03
Yield strength: 6.000e+07

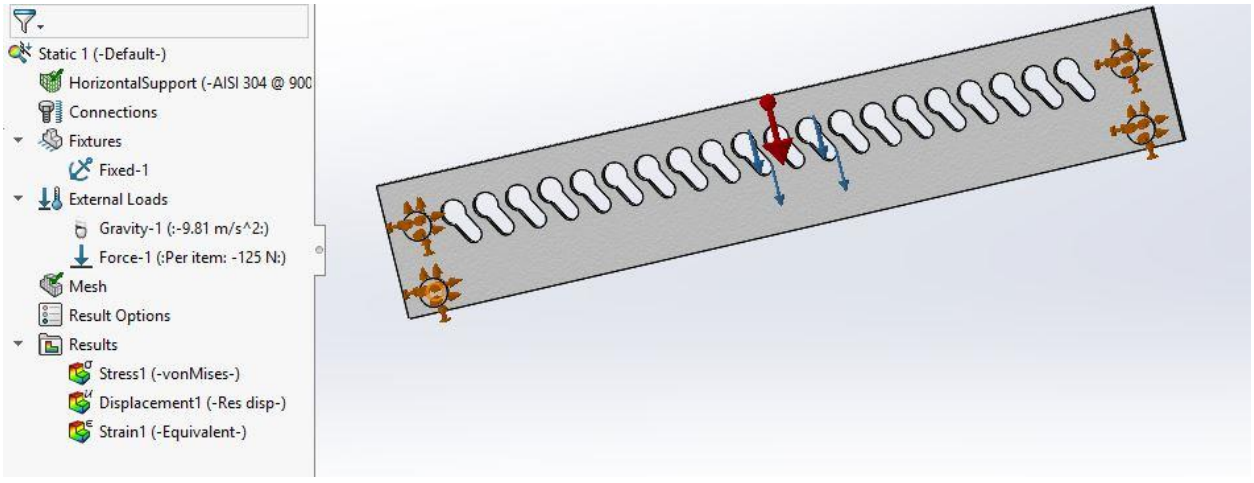
Static 1 (-Default-)
HorizontalSupport (-AISI 304 @ 900
Connections
Fixtures
Fixed-1
External Loads
Gravity-1 (:-9.81 m/s^2:)
Force-1 (:Per item: -125 N:)
Mesh
Result Options
Results
Stress1 (-vonMises-)
Displacement1 (-Res disp-)
Strain1 (-Equivalent-)

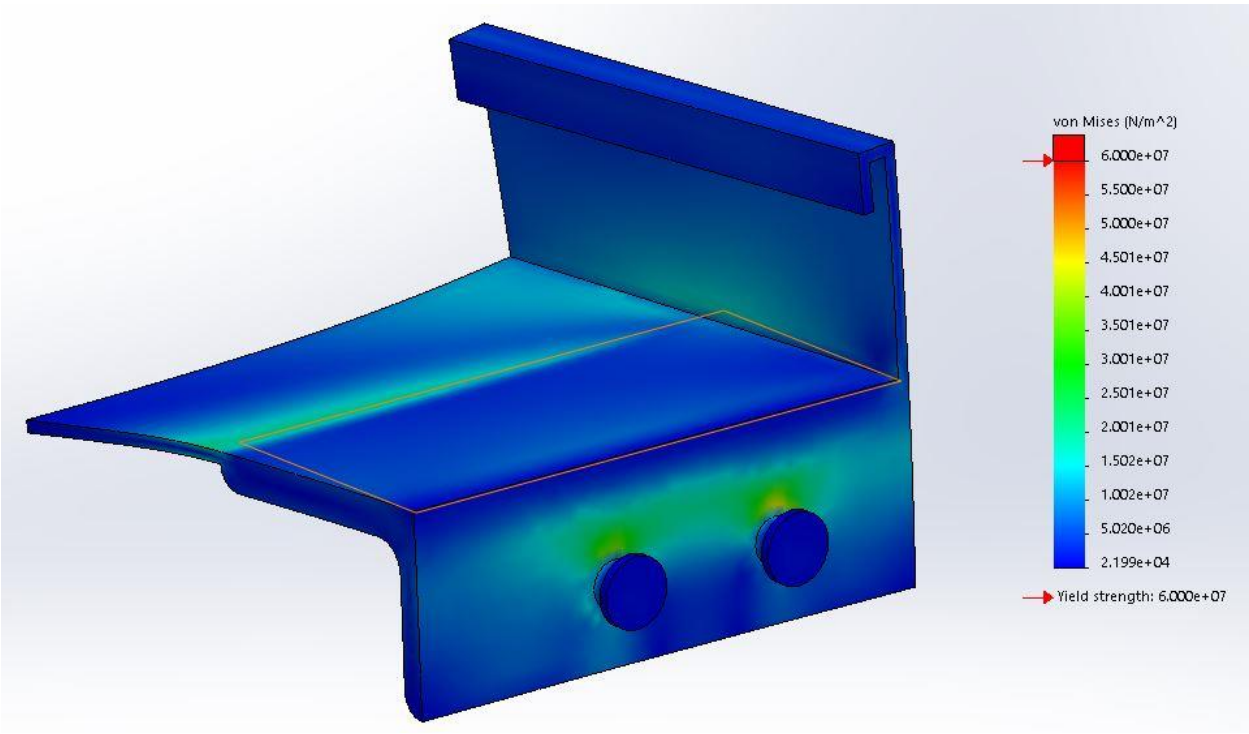
von Mises (N/m^2)
6.000e+07
5.500e+07
5.000e+07
4.501e+07
4.001e+07
3.501e+07
3.001e+07
2.501e+07
2.001e+07
1.502e+07
1.002e+07
5.020e+06
2.199e+04
Yield strength: 6.000e+07

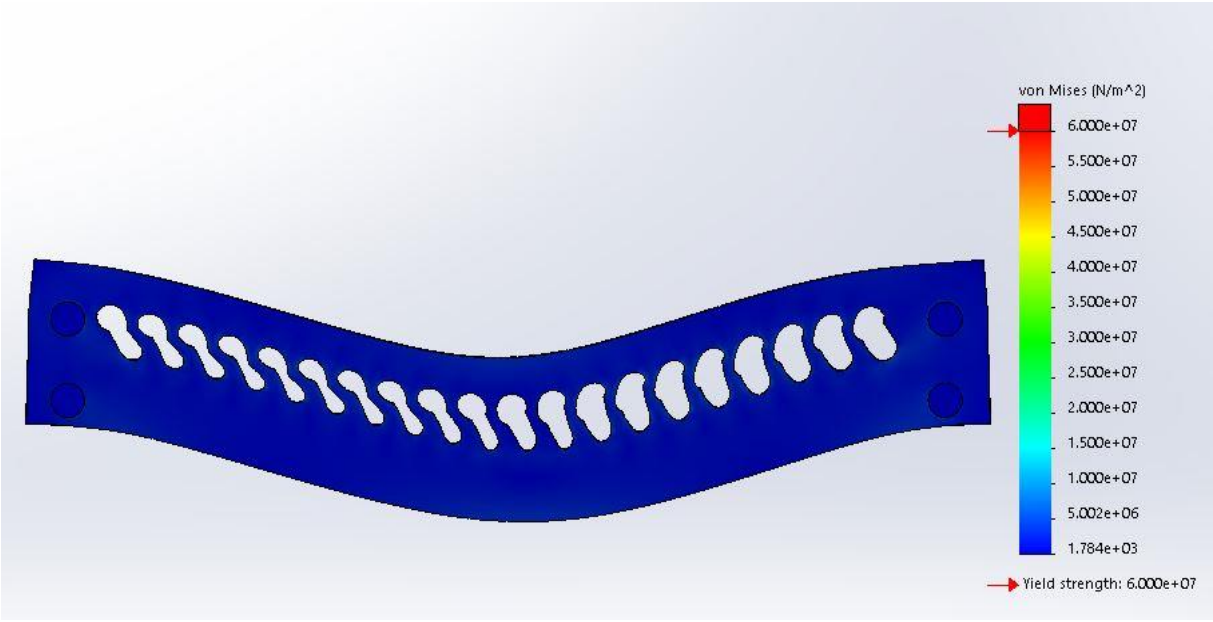
von Mises (N/m^2)
6.000e+07
5.500e+07
5.000e+07
4.500e+07
4.000e+07
3.500e+07
3.000e+07
2.500e+07
2.000e+07
1.500e+07
1.000e+07
5.002e+06
1.784e+03
Yield strength: 6.000e+07

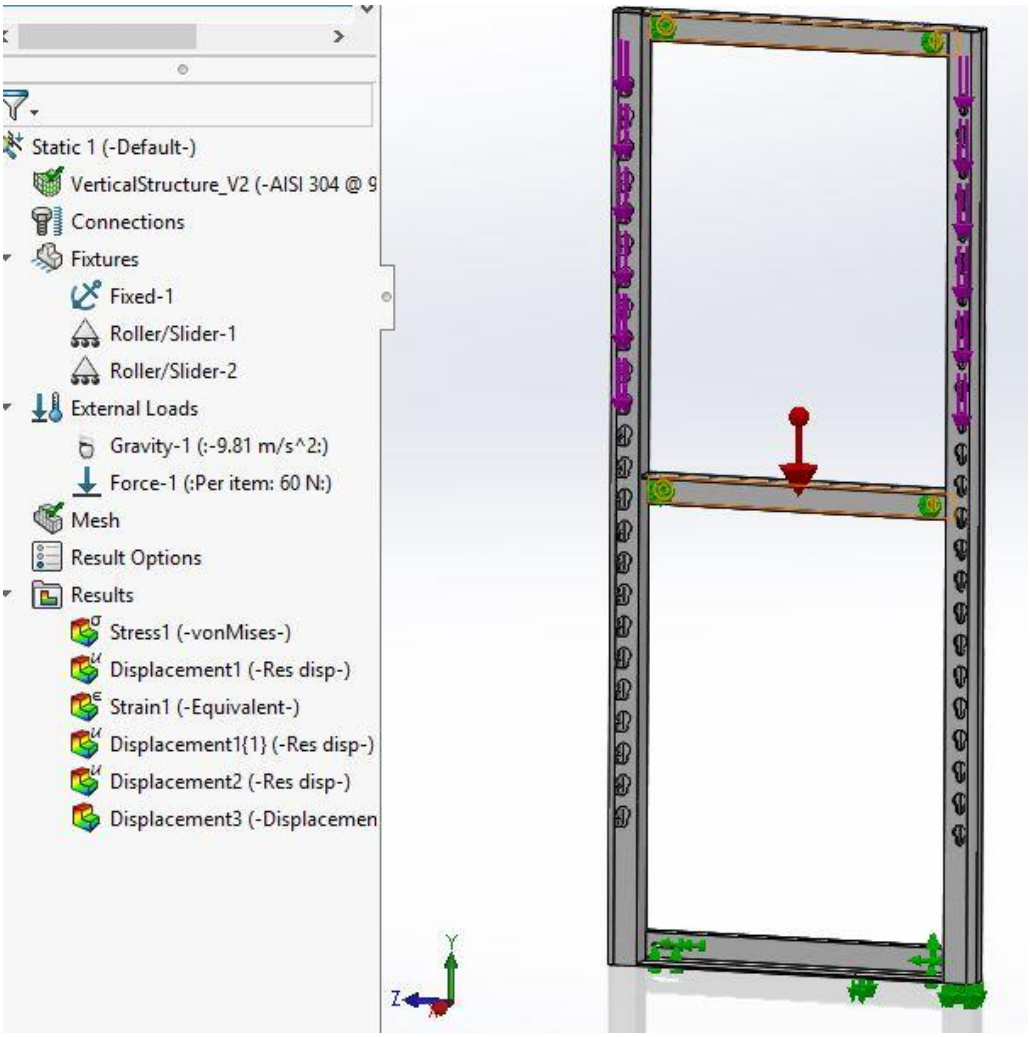
Static 1 (-Default-)
VerticalStructure_V2 (-AISI 304 @ 9
Connections
Fixtures
Fixed-1
Roller/Slider-1
Roller/Slider-2
External Loads
Gravity-1 (:-9.81 m/s^2:)
Force-1 (:Per item: 60 N:)
Mesh
Result Options
Results
Stress1 (-vonMises-)
Displacement1 (-Res disp-)
Strain1 (-Equivalent-)
Displacement1{1} (-Res disp-)
Displacement2 (-Res disp-)
Displacement3 (-Displacemen
Y
Z

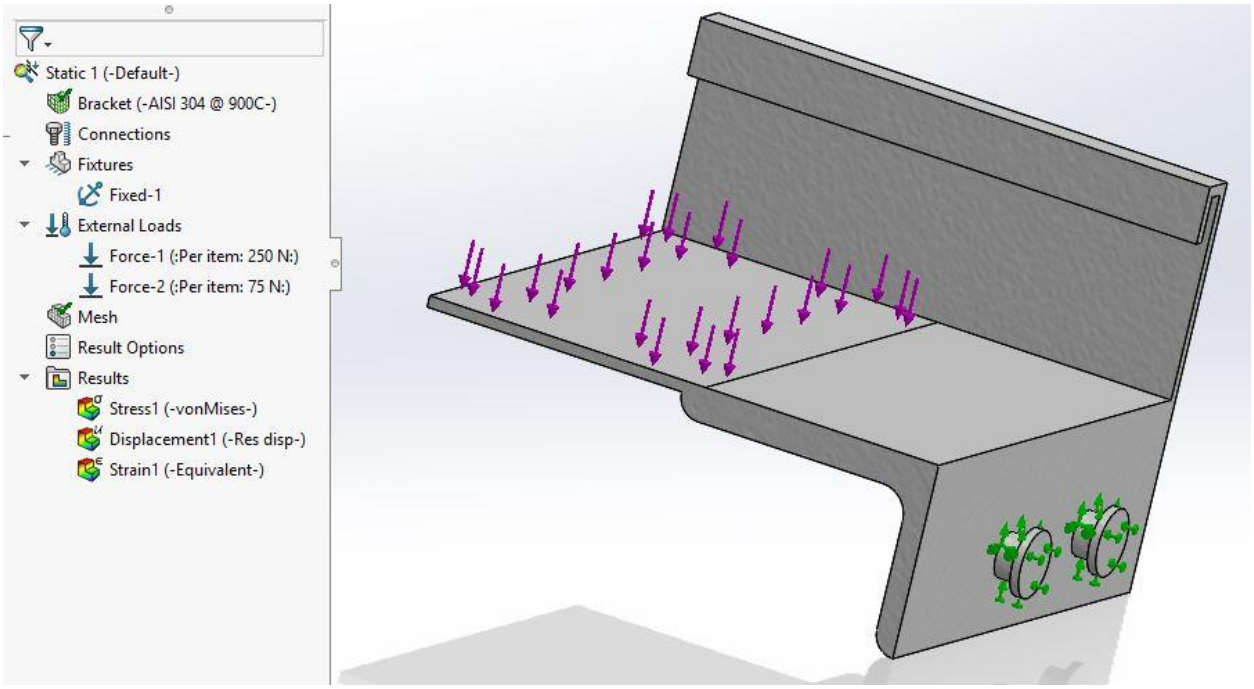
Static 1 (-Default-)
Bracket (-AISI 304 @ 900C-)
Connections
Fixtures
Fixed-1
External Loads
Force-1 (:Per item: 250 N:)
Force-2 (:Per item: 75 N:)
Mesh
Result Options
Results
Stress1 (-vonMises-)
Displacement1 (-Res disp-)
Strain1 (-Equivalent-)

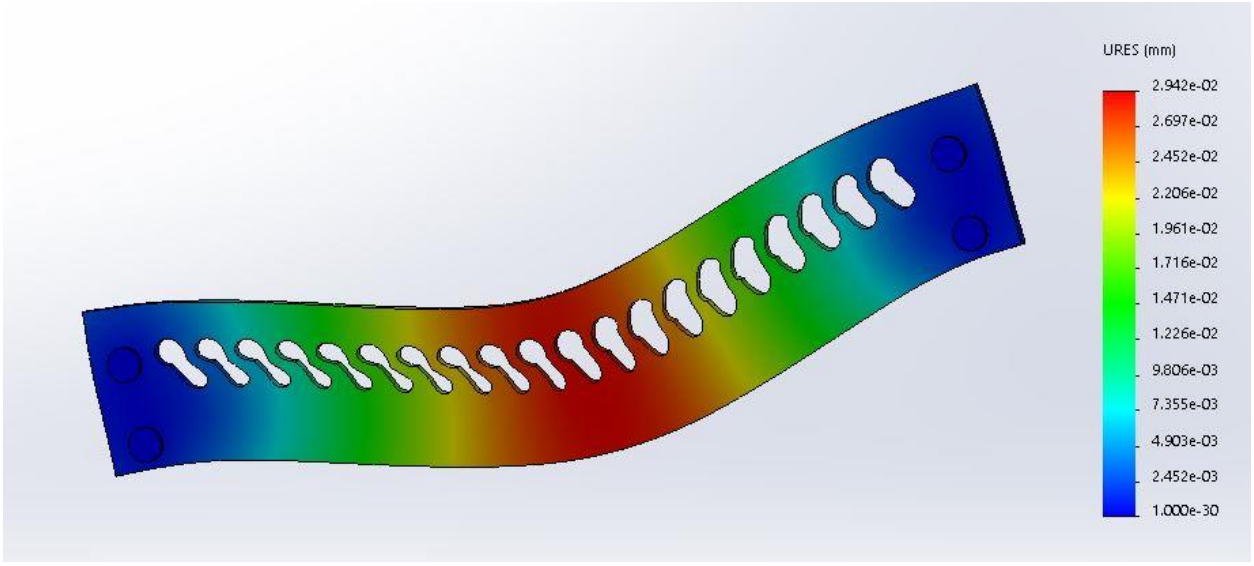
URES (mm)
2.942e-02
2.697e-02
2.452e-02
2.206e-02
1.961e-02
1.716e-02
1.471e-02
1.226e-02
9.806e-03
7.355e-03
4.903e-03
2.452e-03
1.000e-30